6-30-2016

Sensitivity Of The CUORE Detector To Solar Axions

Dawei Li
University of South Carolina

Sensitivity of the CUORE detector to solar axions

by

Dawei Li

Bachelor of Science
Henan University

Submitted in Partial Fulfillment of the Requirements

for the Degree of Doctor of Philosphy in

Physics

College of Arts and Sciences

University of South Carolina

2016

Accepted by:

Richard Creswick, Major Professor

Frank III Avignone, Committee Chairman

Jeff Wilson, Committee Member

Richard Adams, Committee Member

Lacy Ford , Senior Vice Provost and Dean of Graduate Studies

Dedication

Dedicated to my beloved son and wife

Acknowledgments

Without many people's support, advice and encouragement I could not accomplish this degree, so I would like to thank them one by one.

First, I want to give my thanks to Dr. Avignone. Dr. Avignone invited me to join his group and introduced me to the world of neutrinos and axions, changing me from beginner to an experienced person in that field. He is full of energy and wisdom, constantly explaining new stuff and giving suggestions to me. He is also our benefactor, as we graduate students talked in private. I can not finish my thesis without his generous and endless support.

Second, I want to thank Dr. Creswick. Dr. Creswick is my thesis's direct supervisor and co-PI of this project. So we have lots of time to talk about this project and I learned a lot from him. I still remember that every week we will meet several times to talk about how to move forward with this project and how to understand the Peccei-Quinn theory, which is of vital importance for me to understand what we are doing and why we are doing this way. I still remember the times when he and Vicky invited my family to his house to see Christmas tree decorations, have a taste of American Gourmet, enjoy a cup of tea, $\cdots$. I still remember the times when he gave me advice on how to adjust my life in US, even on how to correct my pronunciations. So many good times to enumerate that I couldn't finish them in a single day. So I really appreciate his supports and advices on my study, life and my family. Thank you from the bottom of my heart.

Third, I want to thank my committee members, Dr. Jeff Wilson, Dr. Richard Adams, who is from Chemistry department, for their support, criticism and sugges-

tions.

Then, I want to give a special thank my friends here in the U.S. Nick, my best friend in the US, gave me much support in adjusting to my life in the US and my pronunciation of English. Jason also helped me a lot in seminars and American life. To my SC friends, Hao, Tongtong, Lei, Chris, Clinton, Gary, Rasha, Mat, you guys are awesome and I don't think I could make it through graduate school without your help.

Finally, I want to thank my family.

Abstract

The strong CP problem in Quantum Chromodynamics (QCD), predicts the neutron electric dipole moment to be a factor of 10^{10} larger than the observed upper bound [15]. Roberto Peccei and Helen Quinn [58, 63] proposed an elegant solution to this problem by introducing a global $U(1)_{PQ}$ symmetry that is spontaneously broken at an energy scale f_a. A consequence of this symmetry-breaking is that a new spin-zero neutral pseudoscalar particle, the axion, is generated which is a Nambu-Goldstone boson [70, 78]. The "invisible axion" models with $f_a >> f_{EW}$, typically KSVZ and DFSZ models, have been proposed and recognized to be far-reaching because of the prospect that these axions can be a candidate for dark matter in the universe [59, 1, 27, 25] and the motivation that these axions can be searched for experimentally [19, 12, 29]. Because the axion mass is inversely proportional to the energy scale f_a, invisible axions are very light, very long-lived and very weakly coupled to electrons, photons, nucleons, and quarks, which makes them really difficult to detect directly.

CUORE (Cryogenic Underground Observatory for Rare Events) [10, 7] was originally designed to search for neutrinoless double beta decay ($0\nu\beta\beta$) using a very low background low temperature bolometric detector. It can also be used to search for solar axions and dark matter WIMPs. In this thesis, the potential sensitivity of the CUORE detector to axions produced in the Sun through the Primakoff process and 14.4 keV solar axions emitted by the M1 nuclear transition of ^{57}Fe and detected by the inverse coherent Primakoff process is calculated. The conversion rate is calculated using density functional theory for the electron density and realistic expectations for the background and energy resolution of CUORE. Monte Carlo

calculations for 5 y×741 kg=3705 kg y of exposure are analyzed using the time correlation of individual events with the theoretical time-dependent counting rate. It is found that this exposure can lead to an expected limit on the axion-photon coupling $g_{a\gamma\gamma} < 3.83 \times 10^{-10}\ GeV^{-1}$ for axion masses less than 100 eV for the Primakoff process and an expected model-independent limit on the product of the axion-photon coupling and the axion-nucleon coupling $g_{a\gamma\gamma} g_{aN}^{\text{eff}} < 1.105 \times 10^{-16}$ /GeV for axion masses less than 500 eV for the M1 nuclear transition of ^{57}Fe, with 95% confidence level, respectively.

Preface

"What are axions?" and "Why are they important?" These are the two questions that I am often asked by many people. They are so tightly connected to each other that there is no way to answer one question without mentioning another one. The answers to these two questions were not clear to me until I became familiar to this field with the development of my understanding of the strong CP problem during the advancement of my graduate research.

In the summer of 2013, I had the honor to be on the local organizing committee for the Carolina International Symposium on Neutrino Physics (CISNP). After attending so many talks given by professors with expertise in particle physics from all over the world, I finally realized that the physics of axions is so interesting and that there are so many people devoting their energies to search for axions. Their talks provided me with a bigger vision of this field and motivated me to ponder more on these two questions. So I treat my thesis as an opportunity to explain these two most frequently asked questions in a more easy to understand way.

Another question worth mentioning here is what is the time correlation method and how does it work. I came up with one simple answer to this question when I was driving to Charlotte. Driving on a highway is tedious so you want to turn on the radio to listen some music. Turning on the volume big can guarantee that you can enjoy the music. But at what point is it impossible to distinguish the music from the constant noise that comes from the background if you want to lower down the volume? This is what we used to perform the data analysis and extract useful information from the background counting rate.

Table of Contents

List of Tables

List of Figures

Chapter 1

Standard Model and Strong CP Problem

1.1 $U(1)_A$ problem and the Strong CP problem

Quantum chromodynamics (QCD) is a theory of strong interactions that describes the interactions between quarks and gluons, the force carrier that mediates and transmits the strong force, from which composite particles are built . It predicted so many physical properties that no one doubted the completeness of this theory until the 1970's, when the puzzling $U(1)_A$ problem became particularly clear with the development of QCD. It was found that the QCD Lagrangian for N flavors has a large global symmetry $U(N)_V \times U(N)_A$ when quark masses vanish: $m_f \to 0$. Setting the quark masses to zero for m_u and m_d is reasonable because they are far smaller than $\Lambda_{QCD} \approx 200$ MeV. So these strong interactions should be approximately $U(2)_V \times U(2)_A$ invariant, where the subsripts V and A are vector symmetry and axial-vector symmetry, respectively. Experiments demonstrate that the vector symmetry as a product of isospin and baryon number $U(2)_V = SU(2)_I \times U(1)_B$ is a good symmetry of nature, as shown by the fact that nucleon and pion multiplets exist in the spectrum of hadrons. But it is not true for axial symmetry because it is broken spontaneously since quark condensates occur $< \bar{u}u >=< \bar{d}d > \neq 0$ [57]. Hence no approximate mixed parity multiplets would be expected in the hadronic spectrum and it is evident that there is no lighter state in the hadronic spectrum except $m_\pi \approx 135$ MeV since $m_\eta^2 >> m_\pi^2$. Weinberg suggested that there was no $U(1)_A$ symmetry in the strong interactions [77]. 't Hooft [71] showed that the solution to the $U(1)_A$ problem by the chiral anomaly for axial

currents should use different boundary conditions and the QCD vacuum should have a more complex structure, which makes $U(1)_A$ not a real symmetry of QCD although it is when $m_f \to 0$.

One can easily understand this argument by considering the A_a^0 gauge and realizing that the true vacuum (or θ-vacuum) associated to this gauge is a superposition of n-vacua [57]

$$|\theta >= \sum_n e^{-in\theta}|n >$$

Then the difference in the winding numbers can be written as

$$N|_{t=+\infty} - N|_{t=-\infty} = \frac{g^2}{32\pi^2}\int d\sigma_\mu K^\mu|_{t=-\infty}^{t=+\infty} \tag{1.1}$$

where the integer N is the winding number and K^μ is the Bardeen current. One can rewrite the vacuum to vacuum transition amplitude by using Eq. (1.1)

$$_+ < \theta|\theta >_- = \sum_{M,N} e^{iM\theta}e^{-iN\theta}\ _+ < M|N >_- = \sum_v e^{iV\theta}\sum_N\ _+ < N+V|N >_- \tag{1.2}$$

It can be shown that this difference in winding numbers V is

$$V = \frac{g^2}{32\pi^2}\int d\sigma_\mu K^\mu|_{t=-\infty}^{t=+\infty} = \frac{g^2}{32\pi^2}\int d^4x F_a^{\mu\nu}\tilde{F}_{a\mu\nu} \tag{1.3}$$

Rewriting $_+ < \theta|\theta >_-$ in the path integral representation gives

$$_+ < \theta|\theta >_- = \sum_V \int \sigma A e^{iS_{\text{eff}}[A]}\sigma\left[V - \frac{g^2}{32\pi^2}\int d^4x F_a^{\mu\nu}\tilde{F}_{a\mu\nu}\right] \tag{1.4}$$

where

$$S_{\text{eff}}[A] = S_{\text{QCD}}[A] + \theta\frac{g^2}{32\pi^2}\int d^4x F_a^{\mu\nu}\tilde{F}_{a\mu\nu}$$

Accordingly, the solution to the $U(1)_A$ problem effectively adds to the QCD Lagrangian an extra term:

$$L_\theta = \theta\frac{g^2}{32\pi^2}\int d^4x F_a^{\mu\nu}\tilde{F}_{a\mu\nu} \tag{1.5}$$

where θ is a phase parameter and should be of order unity. This term conserves Charge conjugation (C) invariance but violates Parity (P) and Time reversal (T)

invariance. Hence CP invariance is violated by this term. To make the calculated neutron electric dipole (NED) moment by QCD match the upper bound on NED put by a current experiment[15], θ should be very small, i.e., $\approx 10^{-10}$. But why should the angle θ be so small since it is a strong interaction parameter and should be of order unity? This is known as *the strong CP problem*.

Another way to look at the strong CP problem is to examine the electric dipole moment ($\boldsymbol{d}$) and the magnetic moment ($\boldsymbol{\mu}$) of neutron and see how they behave under three different transformations: 1. Charge conjugation, which changes particles to anti-particles and vice versa. So a particle with charge changes to its anti-particle under Charge conjugation ($C \rightarrow C^*$); 2. Parity, which is said to be even if the state is invariant under its mirror image ($\boldsymbol{r} \rightarrow -r, t \rightarrow t$); 3. Time reversal, is a symmetry that descrbes how an event behaves both as time moves forward and backwards ($t \rightarrow -t, \boldsymbol{r} \rightarrow \boldsymbol{r}$). Local Lorentz invariant quantum field theories like the Standard Model should be symmetric under the product of the three. As shown in figure 1.1, under the Parity transformation, $\boldsymbol{d}$ flips its direction as charges change their positions to opposite ones while $\boldsymbol{\mu}$ remains unchanged. $\boldsymbol{\mu}$ changes its direction as axial current goes backwards under Time reversal while $\boldsymbol{d}$ does not. Because T is violated, CP must be violated to conserve the CPT symmetry.

A quantitative description of the strong CP problem can be performed by doing a rough calculation on the neutron electric dipole moment. The length scale is $\Lambda_{QCD} \approx$ 1 fm. The electric dipole moment will be approximately $d_n \approx \theta \times \frac{1}{3} \times 10^{-15}$ ecm for a quark with charge $\frac{1}{3}e$, where θ here is a free parameter and $0 \leq \theta \leq 2\pi$. But the current experimental bound on the neutron electric dipole moment is $d_n \leq 2.9 \times 10^{-26}$ ecm[15]. So θ should be on the order of 10^{-10} in order for the neutron electric dipole moment predicted by QCD to match up the experimental one. But why should θ be so small since it is a free parameter is known as the strong CP problem.

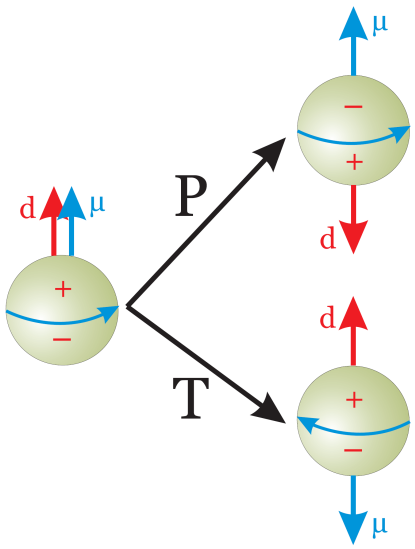

Figure 1.1: Schematic diagram of the electric dipole moment ($\boldsymbol{d}$) and the magnetic moment ($\boldsymbol{\mu}$) of neutron under different transformations. $\boldsymbol{d}$ changes its direction under Parity transformation (P) while $\boldsymbol{\mu}$ remains unchanged. $\boldsymbol{\mu}$ flips its direction under Time reversal (T) while $\boldsymbol{d}$ does not. Since T is violated, the product of Charge conjugation and Parity, or CP should be violated too because CPT symmetry should hold true for all physical phenomena.

1.2 Peccei-Quinn Mechanism

In 1977, Roberto Peccei and Helen Quinn devised an cogent solution to the strong CP problem by introducing a new $U(1)_{PQ}$ global symmetry that is necessarily spontaneously broken at an energy scale f_a, which is an order parameter associated with the $U(1)_{PQ}$ symmetry breaking. As a consequence of this $U(1)_{PQ}$ symmetry breaking, a new neutral spin-zero pseudoscalar particle (Nambu-Goldstone boson) replaces the static CP violating term $\bar{\theta}$ ($\bar{\theta} = \theta + \text{Arg det } M$, M is the quark mass matrix) with a dynamical CP conserving field, the axion.

Under the $U(1)_{PQ}$ transformation, the axion field $a(x)$ transforms by [57]

$$a(x) \rightarrow a(x) + \alpha f_a \tag{1.6}$$

The Lagrangian should be augmented by the axion interaction to make the La-

grangian of the Standard model $U(1)_{PQ}$ invariant:

$$L_{total} = L_{SM} + \bar{\theta}\frac{g^2}{32\pi^2}\int d^4x F_a^{\mu\nu}\tilde{F}_{a\mu\nu} - \frac{1}{2}\partial_\mu a \partial^\mu a + L_{int}[\partial^\mu a/f_a;\Psi] + \xi\frac{a}{f_a}\frac{g^2}{32\pi^2}\int d^4x F_a^{\mu\nu}\tilde{F}_{a\mu\nu} \tag{1.7}$$

The last term in Eq. (1.7) is required to make the $U(1)_{PQ}$ current have a chiral anomaly

$$\partial_\mu J^\mu_{PQ} = \xi\frac{g^2}{32\pi^2}\int d^4x F_a^{\mu\nu}\tilde{F}_{a\mu\nu} \tag{1.8}$$

It also represents an effective potential for the axion field and its minimum is at $< a >= -\frac{f_a}{\xi}\bar{\theta}$ [57]

$$< \frac{\partial V_{\text{eff}}}{\partial a} >= -\frac{\xi}{f_a}\frac{g^2}{32\pi^2} < F_a^{\mu\nu}\tilde{F}_{a\mu\nu} > |_{<a>=-\frac{f_a}{\xi}\bar{\theta}} = 0 \tag{1.9}$$

Because the $\bar{\theta}$-term is cancelled out by this one at the potential minimum, this method provides a dynamical solution to the strong CP problem.

Another way to understand the Peccei-Quinn solution to the strong CP problem is notice that a periodic potential for the axion field, in the effective vacuum angle $\bar{\theta} + \xi\frac{<a>}{f_a}$, is generated when introducing the extra $U(1)_{PQ}$ symmetry [57]:

$$V_{\text{eff}} \approx cos[\bar{\theta} + \xi\frac{< a >}{f_a}] \tag{1.10}$$

Differentiating this potential with respect to $< a >$ gives the PQ solution

$$< a >= -\frac{f_a}{\xi}\bar{\theta}$$

So there will be no CP violating $\bar{\theta}$-term if the Lagrangian in Eq. (1.7) is written in terms of $a_{real} = a - < a >$. Hence the strong CP problem was solved dynamically by the introduction of a global $U(1)_{PQ}$ symmetry. This solution, however, must be tested experimentally by the direct observation of the axions.

Solar Axion Generation and Detection

Solar axions are generated by Primakoff conversion of photons, nuclear M1 transitions, Compton scattering, Bremsstrahlung processes, electron atomic recombination, and by atomic deexcitation. This thesis will focus on the first two processes: the Primakoff effect, in which a photon couples to a virtual photon in the Coulomb field of the nucleus in the solar plasma, producing an axion and the nulear M1 transitions[52, 37, 43]. In the first case the axions have a continuous spectrum with a maximum around the mean energy of 4.2 keV, and die off quickly beyond 10 keV. Axions produced in nuclear transitions are monoenergetic because their energies correspond to the energy difference of specific nuclear transition and can be emitted and escape from the solar core due to the weak interaction between the axion and matter. Solar axions are searched for in magnetic helioscopes[69, 6, 8], by the inverse coherent Bragg-Primakoff process[14, 18], resonant excitation of some nuclide in a laboratory[54, 44], and the axio-electric effect in crystals[30, 48, 13].

Primakoff Conversion

The Primakoff conversion of a photon coupling to a charge through a virtual photon, producing an axion as shown in Figure 1.2(a), has been extensively investigated. While in the inverse Primakoff conversion, an axion couples to a charge via a virtual photon, producing a photon shown in Figure 1.2(b). It has also been widely used in searches for solar axions. Van Bibber et al.[73] carried out a detailed calculation of the solar axion flux, which is similar to black-body radiation and can be well approximated by the empirical form

$$\frac{d\Phi}{dE} = \sqrt{\lambda}\frac{\Phi_0}{E_0}\varphi(E/E_0) \tag{1.11}$$

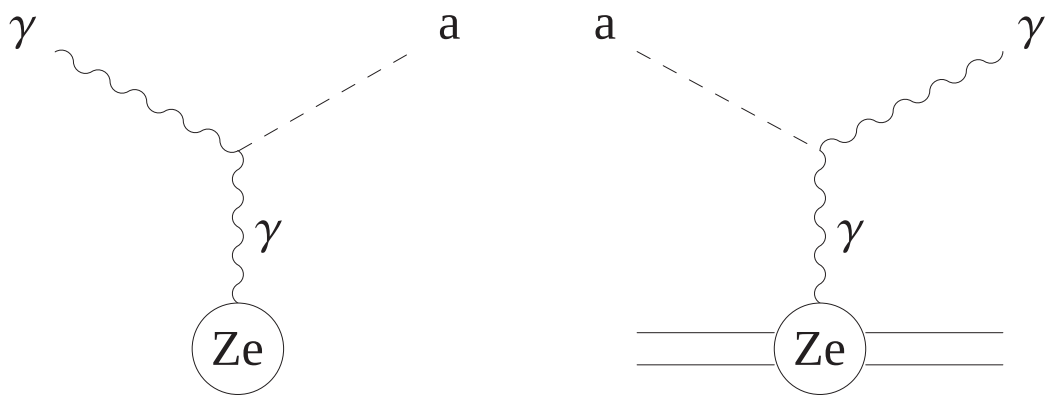

Figure 1.2: (a) An axion is produced in the solar core by the Primakoff effect: A photon couples to a virtual photon in the Coulomb field of the nucleus. (b) An axion couples to a charge in the detector via a virtual photon in the Coulomb field of the crystal producing a photon by the inverse Primakoff effect [14].

where

$$\lambda = (g_{a\gamma\gamma} \times 10^8 GeV)^4 \tag{1.12}$$

is a dimensionless parameter that uses $g_{a\gamma\gamma} = 10^{-8}$ /GeV as a benchmark, $\Phi_0 = 5.95\times10^{14}\ cm^{-2}s^{-1}$ and $\varphi(E/E_0) = \frac{(E/E_0)^3}{\exp(E/E_0)-1}$ [24]. When helium and metal diffusion are included, the core temperature of the solar model will be changed a little. To take into account this small change, we use the adjusted value of $E_0 = 1.103$ keV [24]. Figure 1.3 shows the solar axion flux due to the Primakoff process with $\lambda = 1$. Many solar axions search experiments use the inverse Primakoff conversion. When the incident axions satisty the Bragg condition for a given crystalline plane, as shown in Figure 1.4, coherent conversion of axions to photons can occur

Solar Axions from Nuclear Transitions

The stable isotope ^{57}Fe is found in the solar core with a natural abundance of 2.2% and mass fraction of 2.8×10^{-5}. The first excited state of ^{57}Fe is relatively low and can be thermally excited in the interior of the sun ($kT \approx 1.3$ keV). An excited ^{57}Fe nucleus relaxes to the ground state by emitting a photon with energy 14.4 keV or an

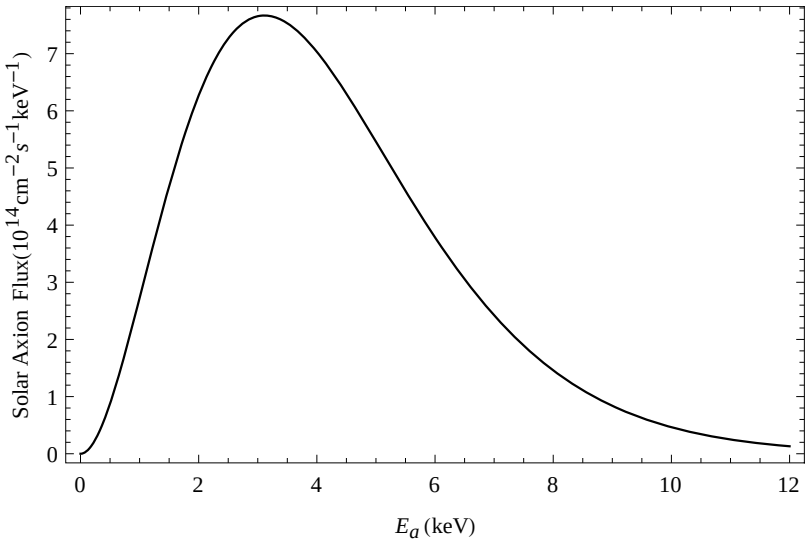

Figure 1.3: Solar axion flux due to Primakoff effect [26]

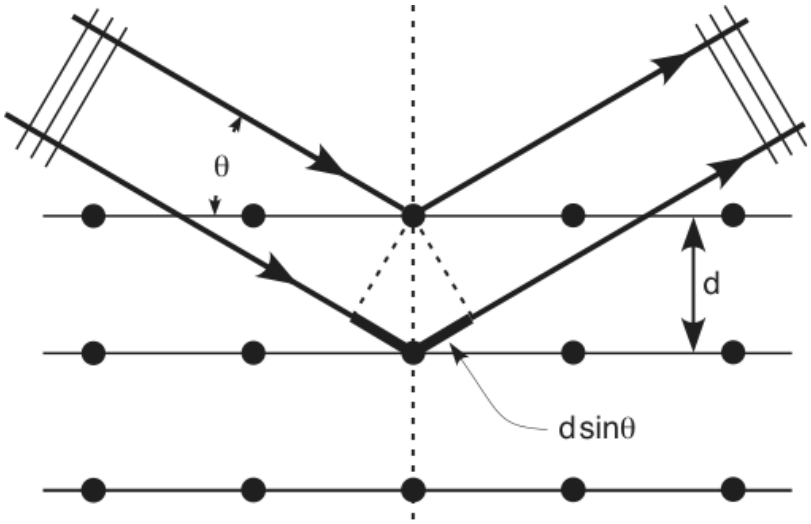

Figure 1.4: Bragg condition

internal conversion electron. It is also possible for the nucleus to decay to the ground state by emitting a 14.4 keV axion. Figure 1.5 is the low energy nuclear energy-level diagram of ^{57}Fe. The mixing ratio of E2 (electric quadrupole with $\delta I = 2$) and M1 (magnetic dipole with $\delta I = 1$) is 0.002, where I is the angular momentum. So the ^{57}Fe nuclear transition is dominated by the M1 transition, hence emission of axions from the M1 nuclear transition is possible. The search for the monoenergetic ^{57}Fe solar axions was given by Moriyama[52] and the flux was calculated by Haxton and

Lee [36]

$$\Phi_{Fe} = 4.56 \times 10^{27} (g_{an}^{eff})^2 / m^2 / s \tag{1.13}$$

where g_{an}^{eff} is the axion-nucleon coupling constant.

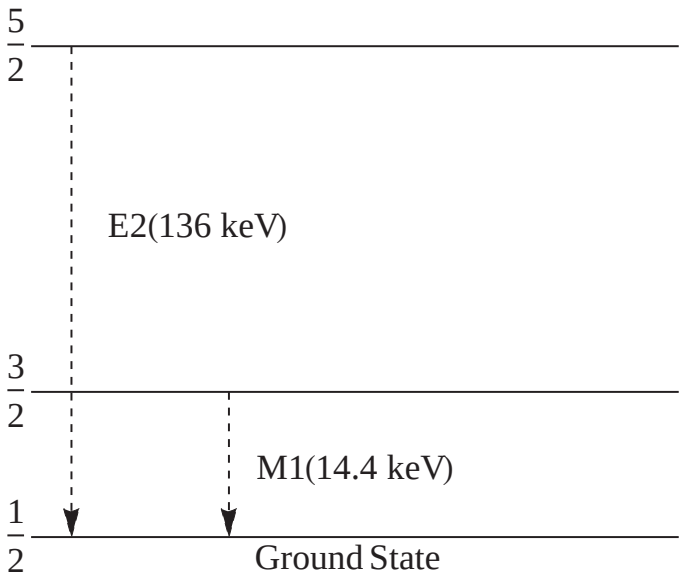

Figure 1.5: Nuclear transiton of ^{57}Fe

Other Axion Emission Processes

Solar axions can also be generated by Compton scattering, Bremsstrahlung processes, electron atomic recombination, atomic deexcitation, and nuclear M1 transitions, all of which are briefly introduced in the following section.

Compton Scattering Process

Figure 1.6 shows the Compton Scattering process. Similar to photon-electron compton effect, an incident phonon interacts with an electron, producing an axion

$$\gamma + e^- \rightarrow a + e^-$$

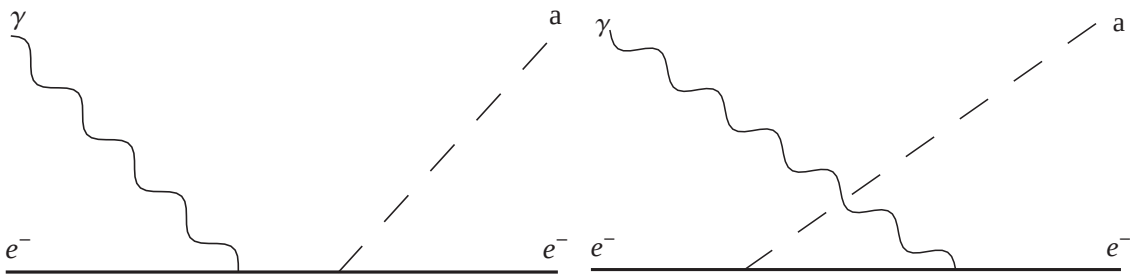

Figure 1.6: Compton scattering.

Bremsstrahlung Process

Figure 1.7 shows a Feynman diagram of Bremsstrahlung emission of axions, the production of axions in electron-nucleus collisions

$$e^- + Ze \rightarrow e^- + Ze + a$$

Another two types of bremsstrahlung are the electron-ion bremsstrahlung (known as

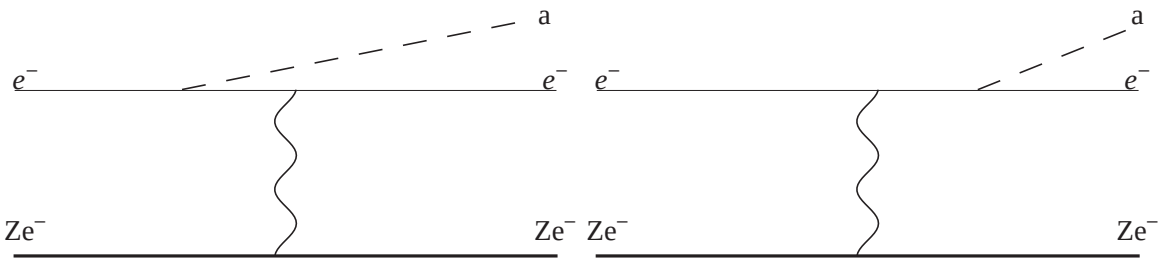

Figure 1.7: Axion Bremsstrahlung.

free-free electron transitions)

$$e + I \rightarrow e + I + a$$

and electron-electron bremsstrahlung

$$e + e \rightarrow e + e + a$$

Electron Atomic Recombination

Electron atomic recombination, also known as free-bound electron transitions or electron capture, is shown in Figure 1.8

$$e^- + I \rightarrow I^- + a$$

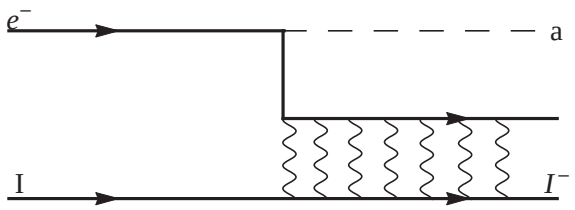

Figure 1.8: Electron Atomic Recombination [64].

Atomic Deexcitation

Atomic deexcitation, or bound-bound electron transitions, is shown in Figure 1.9

$$I^* \rightarrow I + a$$

Figure 1.10 shows a comparison plot of solar axion flux from different generation processes. The blue line corresponds to the Primakoff flux with $g_{a\gamma\gamma} = 10^{-12}$ /GeV. It should be noted that the Primakoff flux is scaled up by a factor of 50 to make it visible. The dot-dashed line is the electron-ion bremsstrahlung, or free-free (FF) electron transition. The solid red line is composed of two parts: the atomic recombination or free-bound (FB) electron transition and atomic deexcitation or bound-bound(BB) electron transition. The black is the total solar axion flux.

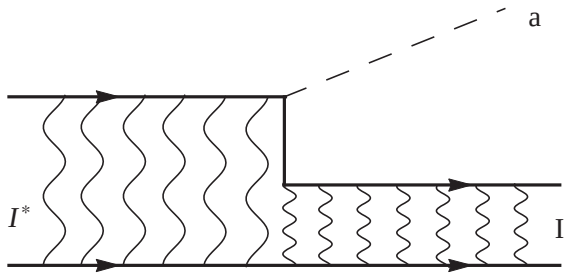

Figure 1.9: Atomic Deexcitation [64].

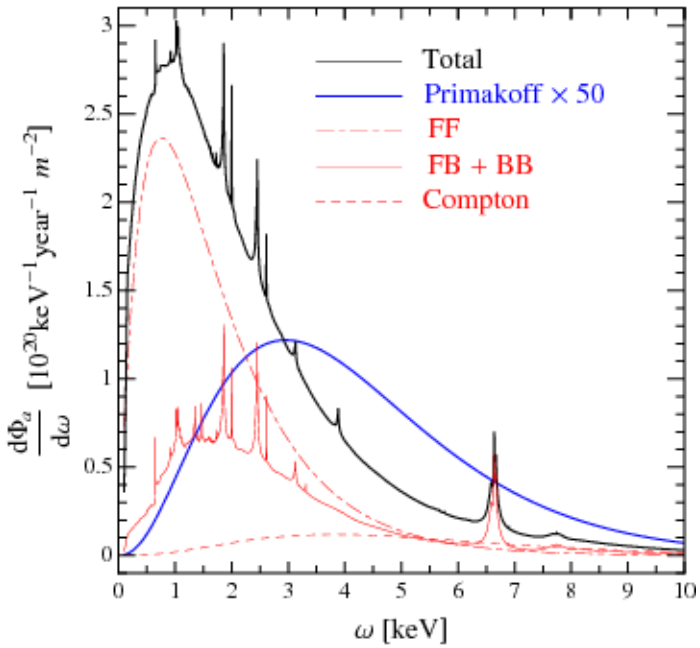

Figure 1.10: The solar axion flux for different processes based on DFSZ model with axion-photon coupling constant $g_{a\gamma\gamma} = 10^{-12}$ /GeV and axion-electron coupling constant $g_{ae} = 10^{-13}$. The dot-dashed line is the free-free (FF) bremsstrahlung. The solid red line is the atomic recombination (free-bound=FB) and atomic deexcitation (bound-bound=BB). The blue line corresponds to the Primakoff flux that is scaled up by a factor of 50 to make it visible. The black line is the total flux.[64]

Axion Bounds

At low energies, the PQ symmetry is explicitly broken because of instanton effects.

Consequently, the axion acquires a small mass through non-perturbation QCD effects

[61],

$$m_a = \frac{z^{1/2}}{1+z}\frac{f_\pi m_\pi}{f_a} = \frac{6.9\ eV}{f_a/10^6\ GeV} \tag{1.14}$$

where $z = m_u/m_d$ is the mass ratio of up and down quarks, $f_\pi = 93$ MeV is the pion decay constant and $m_\pi = 135$ MeV is the pion mass. The phenomenological properties of axions are closely related to those of neutral pions. Although z can vary in the range of $0.3 - 0.6$[79], we stick to most common assumption in the axion literature and take that $z = 0.56$[33, 46]. Early searches for axions have not been successful, due to the assumption that the energy scale of the $U(1)_{PQ}$ symmetry breaking f_a is ralated to the electroweak scale, $f_a \approx f_{EW} = 250$ GeV. These axions were called "standard model axions" and this model was quickly ruled out by experiments[72, 66, 16, 42] in early searches. Models with $f_a >> f_{EW}$ were quickly proposed[41, 68, 80] and recognized to be far-reaching because these axions can be a candidate for dark matter in the universe[59, 1, 27, 25] and can be searched by experiments[69, 19, 12, 29]. Because the axion mass is inversely proportional to f_a, these axions are referred as "invisible" axions, which are very light, very long-lived, very weakly coupled to photons, nucleons, electrons and quarks and accordingly very difficult to detect directly. There are many models for "invisible axions", all of which include at least one electroweak singlet scalar that obtains a vaccum expectation value and thus breaks the $U(1)_{PQ}$ symmetry, but only two are used as generic classes of "invisible" axions in most of the literature, the KSVZ(Kim, Shifman, Vainshtein and Zakharov) or hadronic axions [40, 68] and DFSZ (Dine, Fischler, Srednicki and Zhitnitskij) or GUT axions [80, 28]. The main difference between the two axion models is that the KSVZ axions do not couple to ordinary leptons and quarks at tree-level. In the KSVZ model, new heavy, electrically neutral quarks carry $U(1)_{PQ}$ charges, leaving ordinary leptons and quarks without tree-level axion couplings. While in the DFSZ model, at least two Higgs doublets and ordinary leptons and quarks carry $U(1)_{PQ}$ charges.

The axion interaction scale can be related to that of π^0 from $\frac{f_\pi}{f_a}$ in Eq. (1.14).

One generic property of axions is the two-photon, one-axion interaction that plays a key role in most searches (the Primakoff process),

$$\mathscr{L} = -\frac{1}{4} g_{a\gamma\gamma} F^{\mu\nu} \tilde{F}_{\mu\nu} a = -g_{a\gamma\gamma} \boldsymbol{E} \cdot \boldsymbol{B} a \tag{1.15}$$

where $\mathscr{L}$ is the interaction Lagrangian, $F^{\mu\nu}$ is the electromagnetic field-strength tensor, $\tilde{F}_{\mu\nu}$ its dual, $\boldsymbol{E}$ and $\boldsymbol{B}$ the electric and magnetic fields, a the axion field and $g_{a\gamma\gamma}$ the coupling constant. The axion-photon coupling constant can be written:

$$g_{a\gamma\gamma} = \frac{\alpha}{2\pi f_a} \left(\frac{E}{N} - \frac{2}{3} \frac{4+z}{1+z} \right) = \frac{\alpha}{2\pi} \left(\frac{E}{N} - \frac{2}{3} \frac{4+z}{1+z} \right) \frac{1+z}{\sqrt{z}} \frac{m_a}{m_\pi f_\pi} \tag{1.16}$$

where E and N are the electromagnetic and color anomalies of the axial current associated with the axion field, respectively. In the DFSZ model, $E/N = 8/3$, while in the KSVZ model, $E/N = 0$ if the electric charge of the new heavy quark is taken to be vanishing. Although these models are often treated as generic models, in general E/N is unknown such that it is possible to have a broad range of $g_{a\gamma\gamma}$ [21] for a fixed value of f_a. Taking into consideration the theoretical models and model-dependent factors, we have the "axion band" in the $m_a - g_{a\gamma\gamma}$ plane. Figure (1.11) shows a typical exclusion band of axions with $|E/N - 1.95| = 0.07 - 7$ and constraints achieved by previous experiments [45, 53, 14, 18, 39, 51, 2, 81, 5, 2, 9, 8].

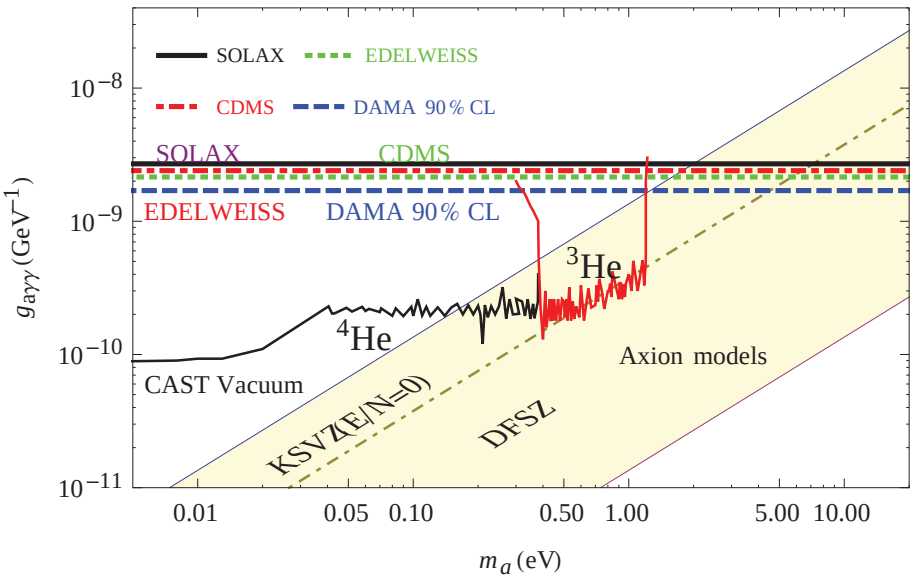

Figure 1.11: Exclusion limits on the $g_{a\gamma\gamma}$-m_a plane by past experiments[45, 53, 14, 18, 39, 51, 81, 5, 2, 9, 8]. The shaded area is favored by the KSVZ [40, 68] and the DFSZ [80, 28] axion models.

Chapter 2

Theory for Direct Detection of Solar Axions: Inverse Primakoff Effect

2.1 Interaction Lagrangian

Axion Field and Vector Potential

The Lagrangian density for electromagnetic and axion fields is

$$\mathscr{L} = \mathscr{L}_a + \mathscr{L}_\gamma + \mathscr{L}_{int}$$

Because axions and photons are bosons, their field operators and Hermitian conjugates, satisfy the canonical commutation relations. For the axion, which is a scalar field, one has

$$[\phi(\boldsymbol{r},t), \pi(\boldsymbol{r}',t)] = i\hbar\delta(\boldsymbol{r}-\boldsymbol{r}') \tag{2.1}$$

$$[\phi(\boldsymbol{r},t), \phi(\boldsymbol{r}',t)] = [\pi(\boldsymbol{r},t), \pi(\boldsymbol{r}',t)] = 0 \tag{2.2}$$

where $\pi(\boldsymbol{r},t)$ is the momentum density conjugate of the axion field and $\phi(\boldsymbol{r},t)$ is the axion field. The axion field $\phi(\boldsymbol{r},t)$ can be written as

$$\phi(\boldsymbol{r},t) = \frac{1}{\sqrt{V}}\sum_{\boldsymbol{p}}\sqrt{\frac{\hbar^2c^2}{2E_a}}e^{i\boldsymbol{p}\cdot\boldsymbol{r}}\left(\phi(\boldsymbol{p})e^{-\frac{iE_at}{\hbar}} + \phi^\dagger(-\boldsymbol{p})e^{\frac{iE_at}{\hbar}}\right) \tag{2.3}$$

which has the dimension of $\sqrt{energy/length}$. For the photon, which has a vector field, one has

$$[A_\alpha(\boldsymbol{r},t), \pi_\beta(\boldsymbol{r}',t)] = i\hbar\delta^{Tr}_{\alpha\beta}(\boldsymbol{r}-\boldsymbol{r}') \tag{2.4}$$

where A_α is the vector potential and $\delta^{Tr}_{\alpha\beta}(\boldsymbol{r}-\boldsymbol{r}')$ is the transverse delta function

$$\delta^{Tr}_{\alpha\beta}(\boldsymbol{r}-\boldsymbol{r}') = \frac{1}{V}\sum_{\boldsymbol{k}}\left(\delta_{\alpha\beta} - \frac{k_\alpha k_\beta}{k^2}\right)e^{i\boldsymbol{k}\cdot(\boldsymbol{r}-\boldsymbol{r}')}$$

and $\partial_\alpha \delta^{Tr}_{\alpha\beta}(\boldsymbol{r}-\boldsymbol{r}') = 0$. In order to derive the eletromagnetic field Lagrangian density, one needs to express $\boldsymbol{E}$ and $\boldsymbol{B}$ in terms of potentials. Maxwell's equations are

$$\begin{aligned} &(1)\quad \nabla\cdot\boldsymbol{E} = \frac{1}{\epsilon_0}\rho, \quad (2)\quad \nabla\times\boldsymbol{E} = -\frac{\partial\boldsymbol{B}}{\partial t}, \\ &(3)\quad \nabla\cdot\boldsymbol{B} = 0, \qquad (4)\quad \nabla\times\boldsymbol{B} = \mu_0\boldsymbol{J} + \mu_0\epsilon_0\frac{\partial\boldsymbol{E}}{\partial t} \end{aligned} \tag{2.5}$$

The fields can be derived from the potentials by

$$\begin{aligned} \boldsymbol{E} &= -\frac{1}{c}\frac{\partial\boldsymbol{A}}{\partial t} - \nabla\phi \\ \boldsymbol{B} &= \nabla\times\boldsymbol{A} \end{aligned} \tag{2.6}$$

where ϕ and $\boldsymbol{A}$ are scalar potential and vector potential, respectively. The most convenient choice is the radiation gauge[23] in this case,

$$\begin{aligned} \phi &= 0 \\ \nabla\cdot\boldsymbol{A} &= 0 \end{aligned} \tag{2.7}$$

So the Lagrangian density for the electromagnetic field in free space is

$$\mathscr{L}_\gamma = \frac{1}{2}\left(\frac{1}{c^2}\left(\frac{\partial\boldsymbol{A}}{\partial t}\right)^2 - (\nabla\times\boldsymbol{A})^2\right)$$

The vector potential can be written in terms of creation and annihilation operators with momentum $\boldsymbol{k}$ and polarization λ

$$A^i(\boldsymbol{r},t) = \frac{1}{\sqrt{V}}\sum_{\boldsymbol{k}\lambda}\sqrt{\frac{\hbar^2c^2}{2E_\gamma}}\epsilon_i(\boldsymbol{k},\lambda)e^{i\boldsymbol{k}\cdot\boldsymbol{r}}\left(a(\boldsymbol{k}\lambda)e^{-\frac{iE_\gamma t}{\hbar}} + (-1)^\lambda a^\dagger(-\boldsymbol{k}\lambda)e^{\frac{iE_\gamma t}{\hbar}}\right) \tag{2.8}$$

so

$$\boldsymbol{B}^i = \frac{i}{\sqrt{V}}\sum_{k\lambda}(\boldsymbol{k}\times\boldsymbol{\epsilon})_i\sqrt{\frac{\hbar^2c^2}{2E_\gamma}}e^{i\boldsymbol{k}\cdot\boldsymbol{r}}\left(a(\boldsymbol{k}\lambda)e^{-\frac{iE_\gamma t}{\hbar}} + (-1)^\lambda a^\dagger(-\boldsymbol{k}\lambda)e^{\frac{iE_\gamma t}{\hbar}}\right) \tag{2.9}$$

The interaction part can be expressed as

$$\mathscr{L}_{int} = g_{a\gamma\gamma}\hbar c\boldsymbol{E}\cdot\boldsymbol{B}\phi \tag{2.10}$$

which has the dimension of *energy/volume*. Finally, the Lagrangian density for the inverse Primakoff conversion of an axion to a photon is

$$\begin{aligned}\mathscr{L} &= \mathscr{L}_a + \mathscr{L}_\gamma + \mathscr{L}_{int} \\ &= \frac{1}{2}\left(\partial_\mu\phi_a\partial^\mu\phi_a - \left(\frac{mc}{\hbar}\right)^2\phi_a^2\right) + \frac{1}{2}\left(\frac{1}{c^2}\left(\frac{\partial \boldsymbol{A}}{\partial t}\right)^2 - (\nabla\times\boldsymbol{A})^2\right) - \frac{\sqrt{\hbar c}}{Mc^2}\boldsymbol{E}\cdot\boldsymbol{B}\phi_a\end{aligned} \tag{2.11}$$

Matrix Element and Conversion Rate

Because $\mathscr{H}_{int} = \mathscr{L}_{int}$, only the interaction term should be considered for the matrix element. In the initial state, one has an axion with momentum $\boldsymbol{p}$ and no photons. While in the final state, one has a photon with momentum $\boldsymbol{k}$, polarization $\boldsymbol{\epsilon}$ and no axions. So the matrix element for such a conversion of an axion with momentum $\boldsymbol{p}$ and energy E_a and to a photon with polarization $\boldsymbol{\epsilon}$ momentum $\boldsymbol{k}$ and energy E_γ is:

$$\mathcal{M} = \langle \boldsymbol{k}\lambda; 0|\mathscr{H}_{int}|0; \boldsymbol{p}\rangle \tag{2.12}$$

The atomic electric field $\boldsymbol{E}$ is given in terms of the charge density distribution $\rho(\boldsymbol{r})$. Performing a Fourier transform on both sides of $\nabla^2\Phi = -\rho$ gives

$$\int_{-\infty}^{\infty} e^{-i\boldsymbol{q}\cdot\boldsymbol{r}}\nabla^2\Phi d^3r = -\int_{-\infty}^{\infty} e^{-i\boldsymbol{q}\cdot\boldsymbol{r}}\rho d^3r$$

Integration by part twice one has

$$\begin{aligned}\int_{-\infty}^{\infty} e^{-i\boldsymbol{q}\cdot\boldsymbol{r}}\nabla^2\Phi d^3r &= \partial_i\Phi e^{-i\boldsymbol{q}\cdot\boldsymbol{r}}|_{-\infty}^{\infty} - \int_{-\infty}^{\infty}\partial_i\Phi\partial_i e^{-i\boldsymbol{q}\cdot\boldsymbol{r}}d^3r \\ &= 0 + i\boldsymbol{q}\int_{-\infty}^{\infty}\partial_i\Phi e^{-i\boldsymbol{q}\cdot\boldsymbol{r}}d^3r \\ &= i\boldsymbol{q}\left(\Phi e^{-i\boldsymbol{q}\cdot\boldsymbol{r}}|_{-\infty}^{\infty} + i\boldsymbol{q}\int\Phi e^{-i\boldsymbol{q}\cdot\boldsymbol{r}}d^3r\right) \\ &= -q^2\tilde{\Phi}(\boldsymbol{q}) \\ &= -\tilde{\rho}(\boldsymbol{q})\end{aligned} \tag{2.13}$$

so $\tilde{\Phi}(\boldsymbol{q}) = \frac{\tilde{\rho}(\boldsymbol{q})}{q^2}$. From $\boldsymbol{E} = -\nabla\Phi$, one can also get $\tilde{\boldsymbol{E}} = \frac{-i\boldsymbol{q}\tilde{\rho}(\boldsymbol{q})}{q^2}$ by using the same method. So finally

$$\begin{aligned}\boldsymbol{E}(\boldsymbol{r}) &= \frac{1}{V}\int \tilde{\boldsymbol{E}} e^{i\boldsymbol{q}\cdot\boldsymbol{r}} d^3\boldsymbol{q} \\ &= \frac{1}{V}\int \frac{-i\boldsymbol{q}\tilde{\rho}(\boldsymbol{q})}{q^2} e^{i\boldsymbol{q}\cdot\boldsymbol{r}} d^3\boldsymbol{q} \\ &= -\frac{1}{V}\sum_{\boldsymbol{q}} i\frac{\boldsymbol{q}}{q^2}\tilde{\rho}(\boldsymbol{q}) e^{i\boldsymbol{q}\cdot\boldsymbol{r}}\end{aligned} \tag{2.14}$$

where in the last step integral is changed to summation. It should be pointed out that $\epsilon_0 = 1$ since we use natural units here. The photon part of the matrix element is

$$\begin{aligned}\langle \boldsymbol{k}\lambda|\mathscr{H}_{int}|0\rangle &= \langle \boldsymbol{k}\lambda|\nabla\times\boldsymbol{A}|0\rangle \\ &= \langle \boldsymbol{k}\lambda|\frac{i}{\sqrt{V}}\sum_{k'\epsilon'}(\boldsymbol{k}'\times\boldsymbol{\epsilon}')_i\sqrt{\frac{\hbar^2c^2}{2E_\gamma}} e^{i\boldsymbol{k}'\cdot\boldsymbol{r}} \\ &\times\left(a(\boldsymbol{k}'\lambda')e^{-\frac{iE_\gamma t}{\hbar}} + (-1)^\lambda a^\dagger(-\boldsymbol{k}'\lambda')e^{\frac{iE_\gamma t}{\hbar}}\right)|0\rangle \\ &= \frac{i}{\sqrt{V}}\sum_{k'\epsilon'}(-1)^\lambda\sqrt{\frac{\hbar^2c^2}{2E'_\gamma}}(\boldsymbol{k}'\times\boldsymbol{\epsilon}')_i e^{i\boldsymbol{k}'\cdot\boldsymbol{r}}\langle \boldsymbol{k}\lambda|a^\dagger(-\boldsymbol{k}'\lambda')|0\rangle \\ &= \frac{i}{\sqrt{V}}\sqrt{\frac{\hbar^2c^2}{2E_\gamma}}(\boldsymbol{k}\times\boldsymbol{\epsilon})_i e^{-i\boldsymbol{k}\cdot\boldsymbol{r}}\end{aligned} \tag{2.15}$$

The axion part of the matrix element is

$$\begin{aligned}\langle 0|\mathscr{H}_{int}|\boldsymbol{p}\rangle &= \langle 0|\frac{1}{\sqrt{V}}\sum_{p'}\sqrt{\frac{\hbar^2c^2}{2E'_a}} e^{i\boldsymbol{p}'\cdot\boldsymbol{r}}\left(\phi(p')e^{-\frac{iE_at}{\hbar}} + \phi^\dagger(-p')e^{\frac{iE_at}{\hbar}}\right)|\boldsymbol{p}\rangle \\ &= \frac{1}{\sqrt{V}}\sum_{p'}\sqrt{\frac{\hbar^2c^2}{2E'_a}} e^{i\boldsymbol{p}'\cdot\boldsymbol{r}}\langle 0|\phi(\boldsymbol{p}')|\boldsymbol{p}\rangle \\ &= \frac{1}{\sqrt{V}}\sqrt{\frac{\hbar^2c^2}{2E_a}} e^{i\boldsymbol{p}\cdot\boldsymbol{r}}\end{aligned} \tag{2.16}$$

So the matrix element becomes:

$$\begin{aligned}\mathcal{M} &= \langle \boldsymbol{k}\lambda; 0|\mathscr{H}_{int}|0; \boldsymbol{p}\rangle \\ &= g_{a\gamma\gamma}\hbar c \int \left(\frac{1}{V}\sum_{\boldsymbol{q}} \frac{-iq_i}{q^2}\tilde{\rho}(\boldsymbol{q}) e^{i\boldsymbol{q}\cdot\boldsymbol{r}} \frac{i}{\sqrt{V}} \sqrt{\frac{\hbar^2c^2}{2E_\gamma}} (\boldsymbol{k}\times\boldsymbol{\epsilon})_i e^{-i\boldsymbol{k}\cdot\boldsymbol{r}} \frac{1}{\sqrt{V}} \sqrt{\frac{\hbar^2c^2}{2E_a}} e^{i\boldsymbol{p}\cdot\boldsymbol{r}} \right) d^3r \\ &= g_{a\gamma\gamma}\hbar c \frac{1}{V^2}\sum_{\boldsymbol{q}} \frac{\hbar^2c^2}{2E_a} \frac{\boldsymbol{q}\cdot(\boldsymbol{k}\times\boldsymbol{\epsilon})}{q^2} \tilde{\rho}(\boldsymbol{q}) \int_V e^{i(\boldsymbol{q}-\boldsymbol{k}+\boldsymbol{p})\cdot\boldsymbol{r}} d^3r \delta(E_a - E_\gamma) \\ &= g_{a\gamma\gamma}\hbar c \frac{1}{V^2}\sum_{\boldsymbol{q}} \frac{\hbar^2c^2}{2E_a} \frac{\boldsymbol{q}\cdot(\boldsymbol{k}\times\boldsymbol{\epsilon})}{q^2} \tilde{\rho}(\boldsymbol{q}) V\delta(\boldsymbol{q}-\boldsymbol{k}+\boldsymbol{p})\delta(E_a - E_\gamma)\end{aligned} \tag{2.17}$$

Taking into account of the first delta function in the above equation one has

$$\begin{aligned}\boldsymbol{q}\cdot(\boldsymbol{k}\times\boldsymbol{\epsilon}) &= \boldsymbol{\epsilon}\cdot(\boldsymbol{q}\times\boldsymbol{k}) \\ &= \boldsymbol{\epsilon}\cdot[(\boldsymbol{k}-\boldsymbol{p})\times\boldsymbol{k}] \\ &= -\boldsymbol{\epsilon}\cdot(\boldsymbol{p}\times\boldsymbol{k})\end{aligned} \tag{2.18}$$

So the matrix element becomes

$$\begin{aligned}\mathcal{M} &= g_{a\gamma\gamma}\frac{\sqrt{\hbar c}}{V}\frac{\hbar^2c^2}{2E_a}\frac{\boldsymbol{\epsilon}\cdot(\boldsymbol{p}\times\boldsymbol{k})}{(\boldsymbol{p}-\boldsymbol{k})^2}\tilde{\rho}(\boldsymbol{p}-\boldsymbol{k})\delta(E_a-E_\gamma) \\ &= g_{a\gamma\gamma}\frac{\sqrt{\alpha}}{2VE_a}\frac{\boldsymbol{\epsilon}\cdot(\boldsymbol{p}\times\boldsymbol{k})}{(\boldsymbol{p}-\boldsymbol{k})^2}\tilde{\rho}(\boldsymbol{p}-\boldsymbol{k})\delta(E_a-E_\gamma)\end{aligned} \tag{2.19}$$

Here the summation over $\boldsymbol{q}$ is performed and the fundamental unit of charge is replaced with the square root of the fine structure constant $\alpha = \frac{e^2}{\hbar c}$ so the charge density is now measured in units of e. It should be pointed out that natural units $\hbar = c = 1$ are used here for convenience. The lowest-order rate for the conversion of an axion with energy E_a and momentum $\boldsymbol{p}$ to a photon with energy E_γ, momentum $\boldsymbol{k}$ and polarization λ is

$$\begin{aligned}T(\boldsymbol{p},\boldsymbol{k}) &= \frac{2\pi}{\hbar}|\langle \boldsymbol{k}\lambda; 0|H_{int}|0;\boldsymbol{p}\rangle|^2 \\ &= g_{a\gamma\gamma}^2\frac{2\pi\alpha}{4V^2E_a^2}|\boldsymbol{\epsilon}\cdot(\boldsymbol{p}\times\boldsymbol{k})|^2\frac{|\tilde{\rho}(\boldsymbol{p}-\boldsymbol{k})|^2}{|\boldsymbol{p}-\boldsymbol{k}|^4}\delta(E_a-E_\gamma)\end{aligned} \tag{2.20}$$

Finally, one needs to sum over all photon final states. For very light axions the energy delta function is equivalent to $|\boldsymbol{p}| = |\boldsymbol{k}|$. The sum over all final states of

photons involves both a summation over polarizations $\boldsymbol{\epsilon}(\boldsymbol{k}\lambda)$ and an integral over the wavevector $\boldsymbol{k}$. Only one polarization vector is parallel to the vector of $\boldsymbol{p} \times \boldsymbol{k}$, hence the sum over polarizations gives us

$$\sum_{\lambda} |\boldsymbol{\epsilon}(\boldsymbol{k}\lambda) \cdot (\boldsymbol{p} \times \boldsymbol{k})|^2 = |\boldsymbol{p} \times \boldsymbol{k}|^2 \tag{2.21}$$

The sum over wavevectors of the photon can be replaced by an integral in the usual way,

$$\textstyle\sum_{\boldsymbol{k}} \rightarrow \frac{V}{(2\pi)^3} \int d^3k$$

which gives us the total conversion rate of an axion with momentum $\boldsymbol{p}$ and a photon with momentum $\boldsymbol{k}$

$$T(\boldsymbol{p}, \boldsymbol{k}) = g_{a\gamma\gamma}^2 \frac{\pi\alpha}{2VE_a^2} \int \frac{d^3k}{(2\pi)^3} \frac{|\boldsymbol{p} \times \boldsymbol{k}|^2}{|\boldsymbol{p} - \boldsymbol{k}|^4} |\tilde{\rho}(\boldsymbol{p} - \boldsymbol{k})|^2 \delta(E_a - E_\gamma) \tag{2.22}$$

Fourier Transform of the Charge Density Distribution

In a crystal, the electron charge density distribution can be treated as the total charge density distribution in a conventional unit cell repeated along lattice vectors

$$\rho(\boldsymbol{r}) = \sum_{\boldsymbol{R}} \rho_c(\boldsymbol{r} - \boldsymbol{R}) \tag{2.23}$$

where $\boldsymbol{R}$ is a lattice vector

$$\boldsymbol{R} = n_1\boldsymbol{a_1} + n_2\boldsymbol{a_2} + n_3\boldsymbol{a_3} \tag{2.24}$$

where a_1, a_2, a_3 are lattice constants and $\rho_c(\boldsymbol{r})$ is the charge density distribution inside the unit cell at the origin. Note that this function by definition vanishes outside the unit cell. The periodicity of the charge density is reflected in the Fourier transform of the charge density distribution:

$$\begin{aligned} \tilde{\rho}(\boldsymbol{q}) &= \int_{v_c} \sum_{\boldsymbol{R}} \rho_c(\boldsymbol{r} - \boldsymbol{R}) e^{-i\boldsymbol{q}\cdot\boldsymbol{r}}\, d^3r \\ &= \left(\sum_{\boldsymbol{R}} e^{i\boldsymbol{q}\cdot\boldsymbol{R}} \right) \tilde{\rho}_c(\boldsymbol{q}) \end{aligned} \tag{2.25}$$

where $\tilde{\rho}_c(\boldsymbol{q})$ is the Fourier Transform of the charge density in a unit cell

$$\tilde{\rho}_c(\boldsymbol{q}) = \frac{1}{v_c}\int \rho(r) e^{-i\boldsymbol{q}\cdot\boldsymbol{r}}\, d^3r$$

The sum $\sum_{\boldsymbol{R}} e^{i\boldsymbol{q}\cdot\boldsymbol{R}}$ can be rewritten as

$$\sum_{\boldsymbol{R}} e^{i\boldsymbol{q}\cdot\boldsymbol{R}} = \sum_{0}^{N_1-1} e^{in_1\boldsymbol{q}\cdot\boldsymbol{a}_1} \sum_{0}^{N_2-1} e^{in_2\boldsymbol{q}\cdot\boldsymbol{a}_2} \sum_{0}^{N_3-1} e^{in_3\boldsymbol{q}\cdot\boldsymbol{a}_3} \tag{2.26}$$

where $N_1N_2N_3 = N_c$, the number of unit cell. Let's take a detour and derive an important equation used here.

$$\begin{aligned} \sum_{n=0}^{N-1} e^{inx} &= \frac{1-e^{iNx}}{1-e^{2iix}} \\ &= \frac{e^{iNx/2}}{e^{ix/2}} \frac{\frac{\sin Nx}{2}}{\frac{\sin x}{2}} \end{aligned} \tag{2.27}$$

When N is approaching to infinity, Eq. (2.27) can be represented by a summation over a series of delta functions,

$$\lim_{N\to\infty} \left| \sum_{n=0}^{N-1} e^{inx} \right| \Rightarrow \sqrt{\pi N} \sum_{k=-\infty}^{+\infty} \delta(x-2\pi k) \tag{2.28}$$

where k is an integer. This function is called the "Dirac Comb". Figure 2.1 shows of $\frac{\sin\frac{Nx}{2}}{\sin\frac{x}{2}}$ with $N = 100$. If we take the modulus squared of Eq. (2.27), we have the Fejer kernal

$$\left| \sum_{n=0}^{N-1} e^{inx} \right|^2 = \frac{\frac{\sin Nx}{2}}{\frac{\sin x}{2}} \cong 2\pi N \sum_{k=-\infty}^{+\infty} \delta(x-2k\pi) \tag{2.29}$$

Using this conclusion one has

$$\left| \sum_{0}^{N_1-1} e^{in_1\boldsymbol{q}\cdot\boldsymbol{a}_1} \right|^2 = 2\pi N_1 \sum_{m_1=-\infty}^{+\infty} \delta(\boldsymbol{q}\cdot\boldsymbol{a}_1 - 2m_1\pi) \tag{2.30}$$

Hence

$$\left| \sum_{\boldsymbol{R}} e^{i\boldsymbol{q}\cdot\boldsymbol{R}} \right|^2 = (2\pi)^3 N_c \prod_{i=1,2,3} \sum_{m_i=-\infty}^{m_i=+\infty} \delta^{(3)}(\boldsymbol{q}\cdot\boldsymbol{a}_i - 2m_i\pi) \tag{2.31}$$

where m_1, m_2 and m_3 are components of $\boldsymbol{m}$. Let $k_i = p_j A_{ji}$, where $\boldsymbol{A}$ can be written as

$$\boldsymbol{A} = \begin{pmatrix} a_{11} & a_{12} & a_{13} \\ a_{21} & a_{22} & a_{23} \\ a_{31} & a_{32} & a_{33} \end{pmatrix}$$

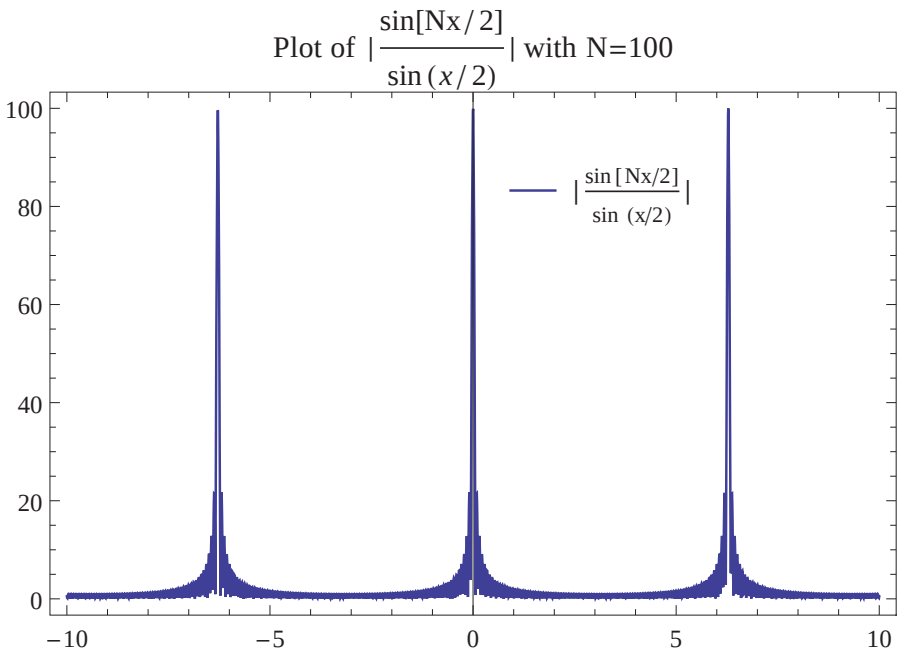

Figure 2.1: A Plot of Dirac Comb

then

$$\begin{aligned}
\delta^{(3)}(\boldsymbol{q}\cdot\boldsymbol{A}-2\boldsymbol{m}\pi) &= \int \frac{d^{(3)}p}{(2\pi)^3} e^{i\boldsymbol{p}\cdot(\boldsymbol{q}\cdot\boldsymbol{A}-2\boldsymbol{m}\pi)} \\
&= \frac{1}{det\boldsymbol{A}} \int \frac{d^{(3)}p}{(2\pi)^3} e^{i\boldsymbol{k}\cdot(\boldsymbol{q}-2\boldsymbol{A}^{-1}\boldsymbol{m}\pi)} \\
&= \frac{1}{det\boldsymbol{A}} \delta^{(3)}(\boldsymbol{q}-2\boldsymbol{A}^{-1}\boldsymbol{m}\pi) \\
&= \frac{1}{det\boldsymbol{A}} \delta^{(3)}(\boldsymbol{q}-\boldsymbol{G}) \\
&= \frac{1}{v_c} \delta^{(3)}(\boldsymbol{q}-\boldsymbol{G})
\end{aligned} \tag{2.32}$$

where $det\boldsymbol{A} = \boldsymbol{a}_1\cdot(\boldsymbol{a}_2\times\boldsymbol{2}_3) = v_c$, the volume of the unit cell, and $\boldsymbol{G} = m_1\boldsymbol{b}_1 + m_2\boldsymbol{b}_2 + m_3\boldsymbol{b}_3$ is a reciprocal lattice vector. The Fourier transform of the charge density is then given by

$$|\tilde{\rho}(\boldsymbol{q})|^2 = |\tilde{\rho}(\boldsymbol{G})|^2 = \frac{(2\pi)^3 N_c}{v_c} \sum_{\boldsymbol{G}} \delta^3(\boldsymbol{q}-\boldsymbol{G}) \, |\tilde{\rho}_c(\boldsymbol{G})|^2 \tag{2.33}$$

Delta Functionality

The conservation of momentum and energy for the inverse Primakoff process gives two delta functions

$$\delta(\boldsymbol{p}-\boldsymbol{k}-\boldsymbol{G})\delta(k^2-p^2-\frac{m_a^2c^2}{\hbar^2})$$

It should be pointed out that the following trick is useful in the delta integral

$$\delta(a^2-b^2)=\delta\left((a+b)(a-b)\right)=\delta\left(2a(a-b)\right)=\frac{1}{2a}\delta(a-b) \tag{2.34}$$

By this trick,

$$\begin{aligned}\delta(k+\frac{E_a}{\hbar c}) &= (k-\frac{E_a}{\hbar c})\delta(k^2-\frac{E_a^2}{\hbar^2c^2}) \\ &= \frac{2E_a}{\hbar c}\delta(k^2-p^2-\frac{m_a^2c^2}{\hbar^2})\end{aligned} \tag{2.35}$$

The integral is then given by

$$\begin{aligned}\int d^3k\delta(\boldsymbol{p}-\boldsymbol{k}-\boldsymbol{G})\delta(k^2-p^2-\frac{m_a^2c^2}{\hbar^2}) &= \delta(|\boldsymbol{p}-\boldsymbol{G}|^2-p^2-\frac{m_a^2c^2}{\hbar^2}) \\ &= \delta[2\boldsymbol{p}\cdot\boldsymbol{G}-G^2+\frac{m_a^2c^2}{\hbar^2}] \\ &= \frac{1}{2\hat{\boldsymbol{p}}\cdot\boldsymbol{G}}\delta[p-\frac{G^2-\frac{m_a^2c^2}{\hbar^2}}{2\hat{\boldsymbol{p}}\cdot\boldsymbol{G}}] \\ &= \frac{p}{G^2-\frac{m_a^2c^2}{\hbar^2}}\delta[p-\frac{G^2-\frac{m_a^2c^2}{\hbar^2}}{2\hat{\boldsymbol{p}}\cdot\boldsymbol{G}}]\end{aligned} \tag{2.36}$$

Finally,

$$\int d^3k\delta(\boldsymbol{p}-\boldsymbol{k}-\boldsymbol{G})\delta(k-\tfrac{E_a}{\hbar c}) = \frac{2pE_a}{\hbar c(G^2-\frac{m_a^2c^2}{\hbar^2})}\delta[p-\frac{G^2-\frac{m_a^2c^2}{\hbar^2}}{2\hat{\boldsymbol{p}}\cdot\boldsymbol{G}}]$$

In the special case where the axion mass is zero(or at least negligible),

$$\int d^3k\delta(\boldsymbol{p}-\boldsymbol{k}-\boldsymbol{G})\delta(k-p) = \tfrac{2p^2}{G^2}\delta(p-\tfrac{G^2}{2\hat{\boldsymbol{p}}\cdot\boldsymbol{G}})$$

Even for a mass as large as 10 eV the correction is only on the order of 2.58×10^{-5} of the zero-mass expression. For an axion with mass 100 eV, the correction is on the order of 2.58×10^{-3}. Therefore it is reasonable to ignore the mass of the axion and

assume it is zero. Note that this is a quite different situation from what found in CAST, where the axion mass causes a loss in coherence as the axion moves down the length of the helioscope.

When the above equation is substituted into the rate one has

$$T(\boldsymbol{p}) = g_{a\gamma\gamma}^2 \frac{4\pi^2 \alpha N_c}{v_c V} \sum_{\boldsymbol{G}} |\tilde{\rho}_c(\boldsymbol{G})|^2 \frac{|\boldsymbol{p} \times \boldsymbol{G}|^2}{G^6} \delta(p - \frac{G^2}{2\hat{\boldsymbol{p}} \cdot \boldsymbol{G}}) \tag{2.37}$$

Meanwhile, the cross section is related to the rate by

$$T(\boldsymbol{p}) = \Phi(\boldsymbol{p}) \sigma(\boldsymbol{p})$$

And the flux of a single axion is $\frac{v_a}{V}$, where v_a is the speed of the axion. For very light axions, $v_a \approx c$, yielding

$$\begin{aligned} \sigma(\boldsymbol{p}) &= g_{a\gamma\gamma}^2 \frac{4\pi^2 \alpha N_c}{v_c} \sum_{\boldsymbol{G}} \left| \frac{\tilde{\rho}_c(\boldsymbol{G})}{G^2} \right|^2 \frac{|\boldsymbol{p} \times \boldsymbol{G}|^2}{G^2} \delta(E_a - E_\gamma) \\ &= g_{a\gamma\gamma}^2 \hbar^3 c^3 \frac{4\pi^2 \alpha N_c}{v_c} \sum_{\boldsymbol{G}} |\tilde{\rho}_c(\boldsymbol{G})|^2 \frac{|\boldsymbol{p} \times \boldsymbol{G}|^2}{G^6} \delta(E_a - E_\gamma) \end{aligned} \tag{2.38}$$

where $\hat{\boldsymbol{p}}$ is the unit vector from the Sun to the detector and $E = \hbar c p$. Note that in the last step $\hbar$ and c are added back in. If we take $g_{a\gamma\gamma} = 10^{-8}$ /GeV, then Eq. (2.38) can be rewritten as

$$\sigma(\boldsymbol{p}) = \frac{\sqrt{\lambda} \hbar c}{(10^8 \text{ GeV})^2} \frac{4\pi^2 \alpha N_c}{v_c} \sum_{\boldsymbol{G}} |\tilde{\rho}_c(\boldsymbol{G})|^2 E_a^2 \frac{|\hat{\boldsymbol{p}} \times \boldsymbol{G}|^2}{G^6} \delta(E_a - E_\gamma) \tag{2.39}$$

where

$$\lambda = (g_{a\gamma\gamma} \times \ 10^8 \text{ GeV})^4 \tag{2.40}$$

is a dimensionless parameter which uses $g_{a\gamma\gamma} = 10^{-8}$ /GeV as a benchmark.

Solar Axion Conversion Rate

The solar axion flux due to the Primakoff conversion has been calculated by van Bibber et al. [73] . This detailed numerical calculation can be well approximated by the empirical form

$$\frac{d\Phi}{dE} = \sqrt{\lambda} \frac{\Phi_0}{E_0} \varphi(E/E_0) \tag{2.41}$$

where $\Phi_0 = 5.95 \times 10^{14}\ cm^{-2}s^{-1}$ and $\varphi(E/E_0) = \frac{(E/E_0)^3}{\exp(E/E_0)-1}$. When helium and metal diffusion are included, the core temperature of the solar model will be changed a bit. To take into account this small change, we use the adjusted value of $E_0 = 1.103$ keV, which is the same value used in our previous paper [24]. The solar-axion spectrum is similar to that of black-body radiation,

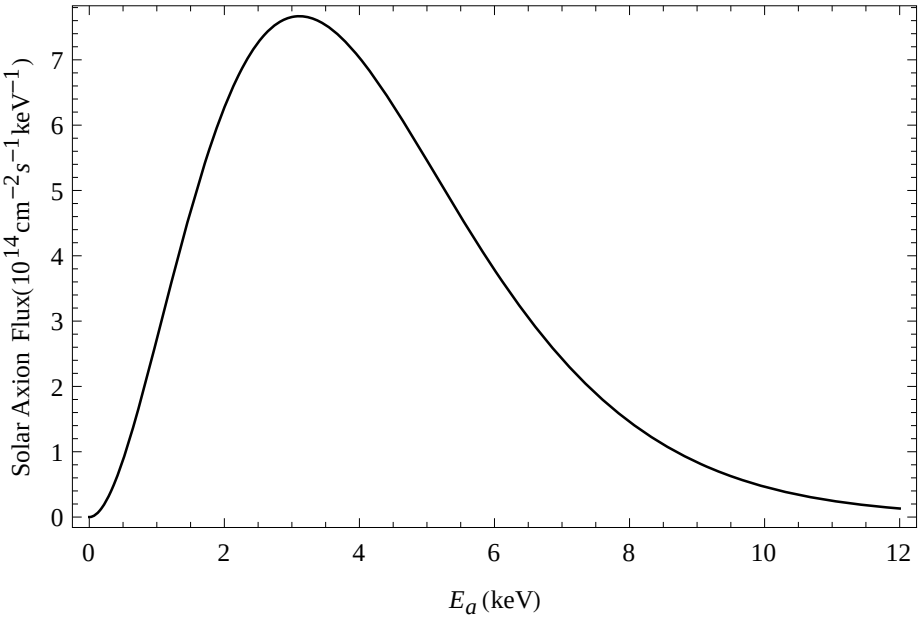

Figure 2.2: Solar axion flux due to Primakoff conversion with $g_{a\gamma\gamma} = 10^{-8}$ /GeV.

Figure 2.2 shows the solar axion flux due to the Primakoff process with $g_{a\gamma\gamma} = 10^{-8}$ /GeV. For convenience, a good order of magnitude estimate for the counting rate can be obtained from the combination of factors

$$\frac{d\dot{N}_0}{dE} = N_A \frac{\Phi_0}{E_0} \left(\hbar c g_{a\gamma\gamma}\right)^2 \lambda = 1.12 \lambda / keV / d \tag{2.42}$$

where N_A is the Avogadro's number. The number of unit cells can be expressed in terms of the mass of the detector m, and molar mass of the unit cell, μ_c

$$N_c = \frac{m}{\mu_c} N_A \tag{2.43}$$

Coherent conversion of axions to photons is possible when the energy of the axion and $\hat{\boldsymbol{p}}$, satisfies the Bragg condition,

$$\epsilon(\hat{\boldsymbol{p}}, \boldsymbol{G}) = \hbar c \frac{G^2}{2\hat{\boldsymbol{p}} \cdot \boldsymbol{G}}$$

where $\hat{\boldsymbol{p}}$ is the unit vector pointing from the core of the Sun to the detector. Taking into account the fact that the detector has a certain energy resolution, we replace the delta function in Eq. (2.38) with a Gaussian function W_Δ with the same full width at half maximum(FWHM)[1] as the detector,

$$\delta(E - \epsilon) \to \frac{1}{\sqrt{2\pi\sigma^2}} e^{-\frac{(E-\epsilon)^2}{2\sigma^2}}$$

and finally we have the conversioin rate

$$\begin{aligned} \frac{d\dot{N}}{dE} &= m\hbar c \frac{d\dot{N}_0}{dE} \frac{4\pi^2\alpha}{\mu_c v_c} \sum_{\boldsymbol{G}} |\tilde{\rho}_c(\boldsymbol{G})|^2 \frac{|\boldsymbol{p} \times \boldsymbol{G}|^2}{G^6} \varphi[\epsilon(\hat{\boldsymbol{p}}, \boldsymbol{G})/E_0] W_\Delta[E - \epsilon(\hat{\boldsymbol{p}}, \boldsymbol{G})] \\ &= m \frac{d\dot{N}_0}{dE} \frac{4\pi^2\alpha}{\mu_c v_c} \sum_{\boldsymbol{G}} |\tilde{\rho}_c(\boldsymbol{G})|^2 \frac{E_a^2}{\hbar c} \frac{|\hat{\boldsymbol{p}} \times \boldsymbol{G}|^2}{G^6} \varphi[\epsilon(\hat{\boldsymbol{p}}, \boldsymbol{G})/E_0] W_\Delta[E - \epsilon(\hat{\boldsymbol{p}}, \boldsymbol{G})] \end{aligned} \tag{2.44}$$

For the germanium detector used by SOLAX[14], $\sigma \sim 0.4$ keV. CUORE will have a characteristic low-energy resolution with FWHM=0.73 keV at 4.7 keV and a low background counting rate [4]. Finally, integrating the total counting rate over a range of energies of width ΔE=0.5 keV gives,

$$R(\hat{\boldsymbol{p}}, E) = \int_{E'}^{E'+\Delta E} \frac{d\dot{N}}{dE}(\hat{\boldsymbol{p}}, E') dE' \tag{2.45}$$

2.2 Tellurium Dioxide Detectors

TeO_2 Crystal Structure and Density Distribution

Tellurium dioxide(TeO_2) has two mineral forms in nature, tellurite (orthorombic) and paratellurite($\alpha - TeO_2$). The latter is used by CUORE and has a tetragonal symmetry with space group $D_4(422)$ and can be treated as a distorted rutile structure

[1] $FWHM = \lambda_+ - \lambda_- = 2\sqrt{2ln2}\sigma \approx 2.3548\sigma$

with lattice constants $a = b = 4.8088$ Å and $c = 7.6038$ Å [20]. TeO_2 was chosen by CUORE to study neutrinoless double beta decay using four criteria: First, TeO_2 crystals have very low heat capacity at low temperature. Since CUORE will use the bolometric technique, which determines the energy deposited in the crystal by a radioactive decay by measuring the temperature increase, the heat capacity of the crystal should be very low. According to the Debye law, at very low temperature, the specific heat is proportional to $(T/T_D)^3$. For TeO_2 crystals, $T_D = 232K$[50], which yields an extremely low heat capacity at low temperature and good energy resolution. Second, the thermal expansion coefficient of TeO_2 crystal[35] is close to that of copper frame used as a mechanical support of the detector, resulting in less strain on the crystals during the cooling process. Third, but not the most important, ^{130}Te has a very high natural abundance, 33.8%, which eliminates the need for expensive and complicated enrichment processes. Finally, the $\alpha - TeO_2$(also used by CUORE) is commercially produced on a large scale due to its useful acousto-optic properties can can be grown into large high-quality single crystal, which further reduces the cost of the detector.

Table 2.1: Relative coordinates of atoms in a conventional unit cell of TeO_2 crystal with respect to lattice constants a, a, c.

Element	a_r	b_r	c_r
O	0.13933	0.24991	0.19288
O	0.86067	0.75009	0.69288
O	0.25009	0.63933	0.44288
O	0.74991	0.36067	0.94288
O	0.36067	0.74991	0.05712
O	0.63933	0.25009	0.55712
O	0.24991	0.13933	0.80712
O	0.75009	0.86067	0.30712
Te	0.01565	0.01565	0.0
Te	0.98435	0.98435	0.5
Te	0.48435	0.51565	0.25
Te	0.51565	0.48435	0.75

Table 2.1 shows the relative coordinates of O and Te atoms in a conventional unit cell of TeO_2 with respect to lattice constants a, a, c. The front and top views of the TeO_2 crystal structure is shown in figure 2.3. And the contour of the charge density distribution on the X-Y (z=0) plance can be seen from fiigure 2.4.

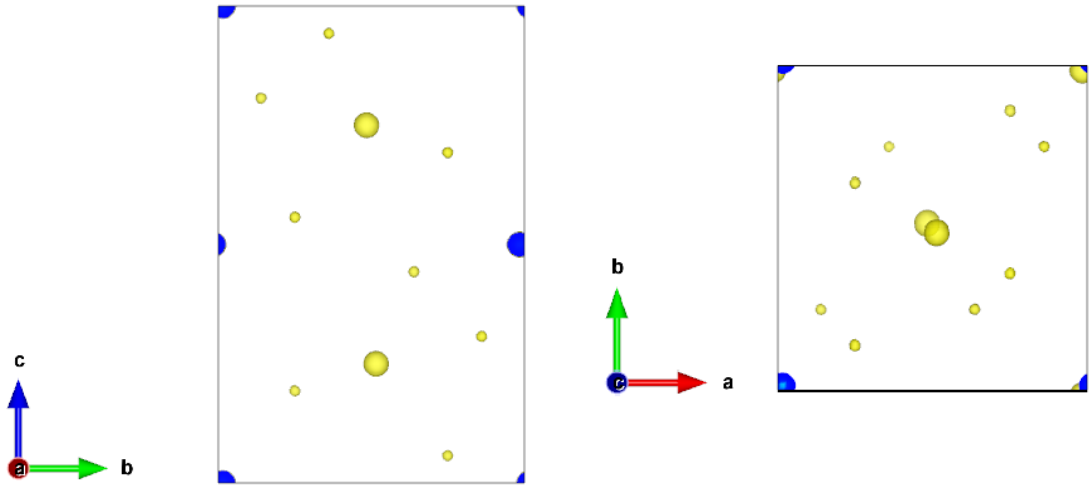

Figure 2.3: Front and top views of the TeO_2 crystal structure, calculated with the software VESTA.

The Fourier transform of the charge density distribution for a given reciprocal lattice vector $\boldsymbol{G}$ can be calculated by density functional theory (DFT) or by using the screened Coulomb approximation (SCA) [24]. Table. 2.2 shows the comparisons between the two. It can be seen that $|\tilde{\rho}(\boldsymbol{G})|^2$ calculated by SCA is larger than that given by DFT, which means that SCA yields a higher conversion rate and thus a higher counting rate. Consequently, it gives a more strict bound on the coupling constant $g_{a\gamma\gamma}$ in the case of a null result.

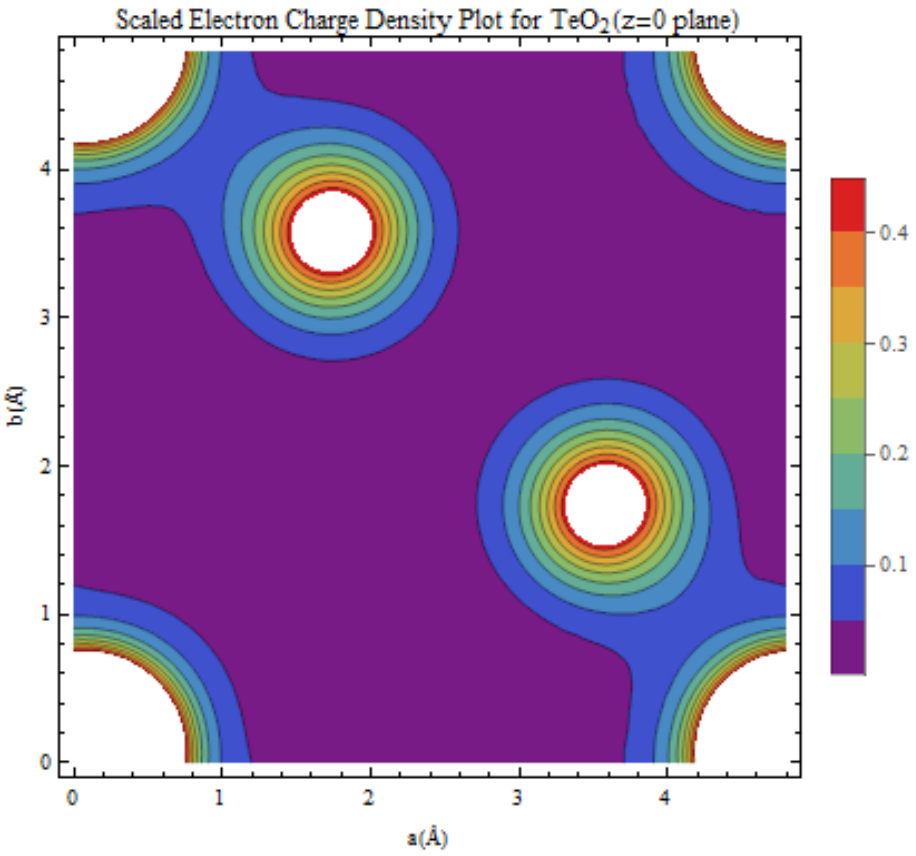

Figure 2.4: Contour plot of TeO_2 electron density distribution on z=0 plane.

2.3 Counting Rates

Position of the Sun

Mathematica was used calculate the altitude and azimuth for the Sun, (θ,φ). The altitude is the angle between the vector from an observer to the Sun and the reference

[2]The integers (h, k, l) are the components of reciprocal lattice vectors $\boldsymbol{G} = 2\pi(\frac{h}{a}, \frac{k}{a}, \frac{l}{c})$.

[3]d is the distance between Bragg planes for a given $\boldsymbol{G}$ and $d = 2\pi/G$.

[4]E_0 is the minimum energy for which a zero rest mass particle can Bragg scatter with momentum transfer $\boldsymbol{G}$.

[5]*mult* is the multiplicity, or the number of reciprocal lattice vectors in each family of planes.

[6]$|\tilde{\rho}_c^{DFT}(\boldsymbol{G})^2|$ is the Fourier transform of the charge density distribution ρ calculated by WIEN2k based on density functional theory.

[7]$|\tilde{\rho}_c^{SCA}(\boldsymbol{G})^2|$ is Fourier transform of the charge density distribution ρ based on screening length [24].

Table 2.2: Selected reciprocal lattice vectors that contribute to the inverse Primakoff conversion of solar axions in TeO_2.

$(h,k,l)^2$	$d(\text{Å})^3$	$E_0(\text{keV})^4$	$mult^5$	$\lvert\tilde{\rho}_c^{DFT}(\boldsymbol{G})^2\rvert^6$	$\lvert\tilde{\rho}_c^{SCA}(\boldsymbol{G})^2\rvert^7$
(1,1,1)	3.0889	2.01	8	72.53	118.98
(2,2,1)	1.6536	3.75	8	505.88	1021.16
(1,2,3)	1.6265	3.81	16	220.69	663.13
(4,2,0)	1.0723	5.78	8	10620.90	29125.90
(3,2,3)	1.1737	5.28	16	481.43	1988.35
(3,4,1)	0.9513	6.52	16	1280.11	3818.14
(3,3,3)	1.0296	6.02	8	435.17	2787.61
(2,3,4)	1.0842	5.72	16	363.21	114.08
(1,5,2)	0.9121	6.80	16	24.71	80.38
(4,2,4)	0.9304	6.66	16	9969.21	30530.90
(2,3,5)	0.9944	7.39	16	549.24	2118.81
(5,4,1)	0.7452	8.32	16	1641.36	5967.68
(5,3,3)	0.7811	7.94	16	2411.45	5240.20
(1,3,6)	0.9635	6.43	16	15.98	30.00
(3,4,5)	0.8076	7.68	16	3339.10	3984.78
(1,5,5)	0.7964	7.78	16	2271.45	4415.45
(6,1,4)	0.7265	8.53	16	243.03	117.57
(3,3,6)	0.8377	7.40	8	47.86	273.31
(7,2,2)	0.6487	9.56	16	13981.86	23033.10
(6,0,5)	0.7051	8.79	8	984.16	6131.84
(2,3,7)	0.8335	7.44	16	1540.88	2226.21
(1,1,8)	0.9021	6.87	8	11543.29	36814.40
(4,4,6)	0.7012	8.84	8	238.77	855.70
(7,2,4)	0.6514	9.98	16	765.01	622.35
(6,1,6)	0.6665	9.30	16	9789.80	27343.1
(7,0,5)	0.6230	9.95	8	1261.85	8147.2
(6,3,6)	0.6203	9.99	16	14051.54	25538.9

plane[8],and the azimuth is the angle between the reference direction (North) and the line from the observer to the Sun projected onto the same reference plane.

$$-\frac{\pi}{2} \leq \theta \leq \frac{\pi}{2}, 0 \leq \varphi \leq 2\pi$$

In the Cartesian coordinate system, the East direction of the reference plane is chosen as the X-axis and North as the Y-axis. So the Z-axis is pointing upward. The position

[8]The observer's local horizon or the surface of the sea

of the Sun in this reference frame is $R_{\odot}\,(cos\theta sin\varphi, cos\theta\cos\varphi, sin\theta)$, where $R_{\odot}$ is the distance from the Earth to the Sun. Consequently, the unit vector from the Sun, $\hat{p}$ is

$$\hat{p} = (-cos\theta sin\varphi, -cos\theta\cos\varphi, -sin\theta) \tag{2.46}$$

One could sample the position of the Sun every minute, or even every hour, then calculate the instant counting rate at these sampling points and interpolate them to get a continuous counting rate. If it is appropriate to choose a longer time interval to sample the position of the Sun without losing much information, then a longer time interval seems better, since it can shorten the calculation time. So it is interesting to see how different sampling time intervals affect the counting rates. For comparison, the counting rates for two energy bins with different sampling time intervals (2 mins, 5 mins, 10 mins and 15 mins) are calculated. Figure 2.5 and figure 2.6 show the counting rates for different sampling time intervals. It is easy to see that longer sampling time intervals tend to smooth peaks where there might exist higher instantaneous counting rates, while for other regions, they overlay on each other so no information will be lost.

So the only region where one might lose some counts is in the peaks. It is worthwhile to see how large the differences are by integrating these counting rates over a single day. Table 2.3 shows the comparison of total counts over a single day for different choices of sampling time intervals.

Table 2.3: Comparison of counts with different Δt.

$\Delta t(min)$	C/kg/d$(2.5-3.0keV)$	C/kg/d$(4.5-5.0keV)$	Total Counts for 16 bins
2	5.36936	20.6101	200.431
5	5.36937	20.6103	200.283
10	5.36932	20.5989	200.562
15	5.36925	20.6421	200.935

From these two comparison plots and the table, it is easy to conclude that 5-minute

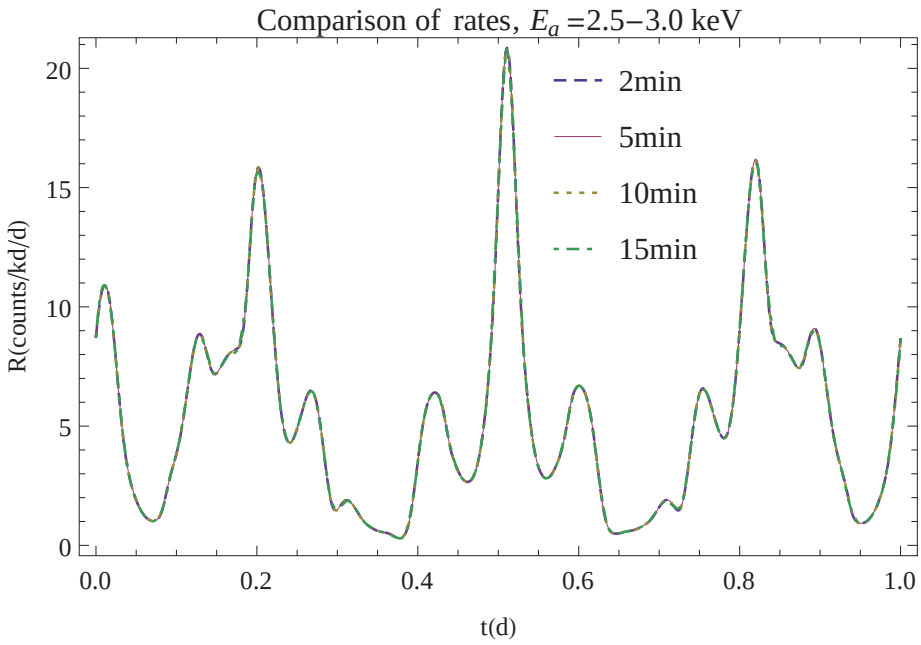

Figure 2.5: Comparison of rates with different Δt

sampling time intervals are sufficiently small to ensure that not much information will be lost. Accordingly, 5-minute sampling times were chosen to calculate the other rates with different energies.

Will the distance from the Sun to the Earth affect the counting rate? This is another question needed to be addressed here. The distance from the Earth to the Sun is 1.496×10^8 km. The Solar radius is $r_\odot = 6.955 \times 10^5$ km and solar core is $0.2 \sim 0.25 r_\odot$, or $1.391 \sim 1.739 \times 10^5$ km. So the solar core subtends an angle of $0.053^\circ - 0.066^\circ$ with respect to the Earth. Meanwhile, the Sun moves 0.25°/min. The speed of light is 2.99×10^5 km/s, so it takes axions 500 seconds to get to the Earth. During this time, the Sun can move 2°. Here a question arises. Is the position of the Sun we record 500 seconds ago or is it instantaneously? The answer is if the mass of the axion is relatively small, then it doesn't matter. The following is the approximation used to address this question. The energy of the axion is

$$E = \sqrt{(pc)^2 + (mc^2)^2} \tag{2.47}$$

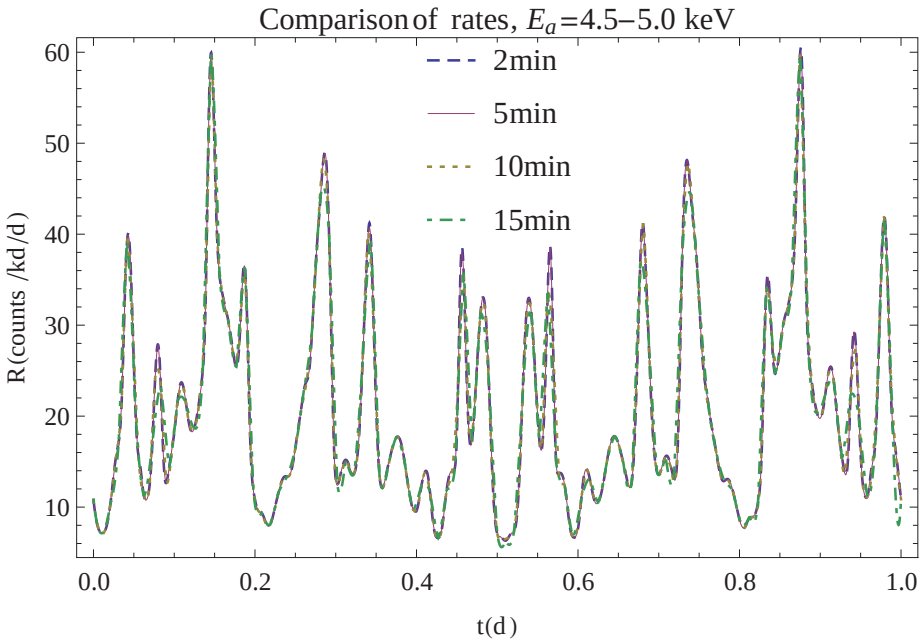

Figure 2.6: Comparison of rates with different Δt

The speed of axion is

$$V = \frac{\partial E}{\partial p} = \frac{pc^2}{E} \tag{2.48}$$

so

$$pc = \sqrt{E^2 - (mc^2)^2} \approx E[1 - \frac{1}{2}(\frac{mc^2}{E})^2] \tag{2.49}$$

The time it takes for the axion to reach to the Earth is

$$\begin{aligned} T = \frac{L}{V} &= \frac{L}{c}\frac{c}{V} \\ &= \frac{L}{c}\frac{E}{pc} \\ &= T_0(1 + \frac{1}{2}(\frac{mc^2}{E})^2) \end{aligned} \tag{2.50}$$

where T_0 is the time a photon takes to get to the Earth. The energy of axions is in the range of keV, if the mass of axion is 1 eV, then the second term in T is $0.5 \times 10^{-6} T_0$, which means it is negligible compared with T_0. If the the mass of axion is 100 eV, then 0.5 percent of T or 2.5 s is also small, but during this time, the Sun moves 0.01°, not negligible compared with the solar core size. However, axions with mass of 100 eV would be heavy axions.

Energy-dependent Counting Rates with 16 Energy Bins

Starting from the counting rate expression in Eq. (2.45), and substituting all parameters in, the counting rates in the units of $counts/kg/d$ over a range of energies $E_a = 2 \sim 10$ keV are calculated. Figure 2.7 shows the counting rates as a function of

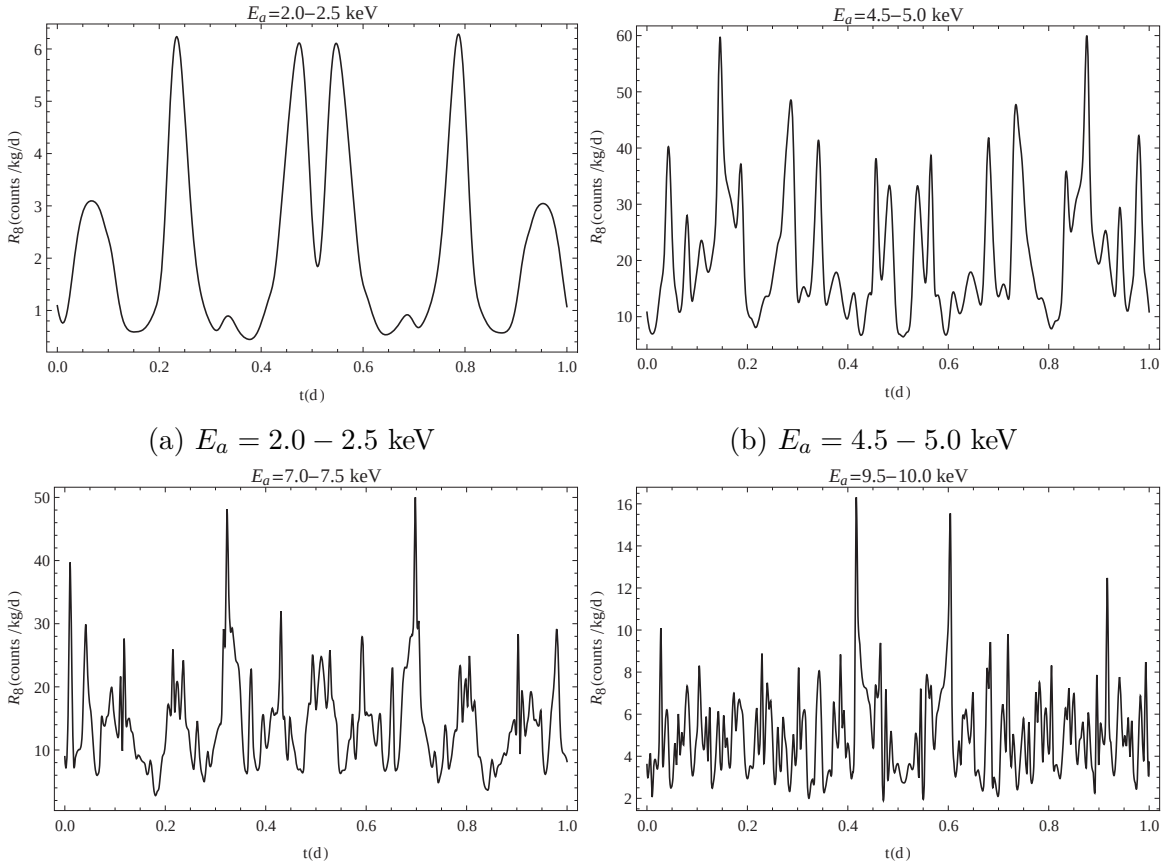

(a) $E_a = 2.0 - 2.5$ keV (b) $E_a = 4.5 - 5.0$ keV

(c) $E_a = 7.0 - 7.5$ keV (d) $E_a = 9.5 - 10.0$ keV

Figure 2.7: Expected counting rates $R_8(E, t)$ of photons produced by the inverse Primakoff conversion of solar axions in the CUORE detector, which is located at the Laboratori Nazionali del Gran Sasso(LNGS) in central Italy(42°28′N 13°33′E). The rates were calculated for $g_{a\gamma\gamma} = 10^{-8}$/GeV [26] .

time over a single day for several energy intervals. One way to understand the time-dependent counting rate is that at any instant there might be one or more reciprocal lattice vectors satisfying the Bragg condition. If one considers the contribution to the counting rate of a single $\boldsymbol{G}$, one can imagine isodetection contours projected on the celestial sphere. Figure 2.8 shows the isodetection contours for axions with energies

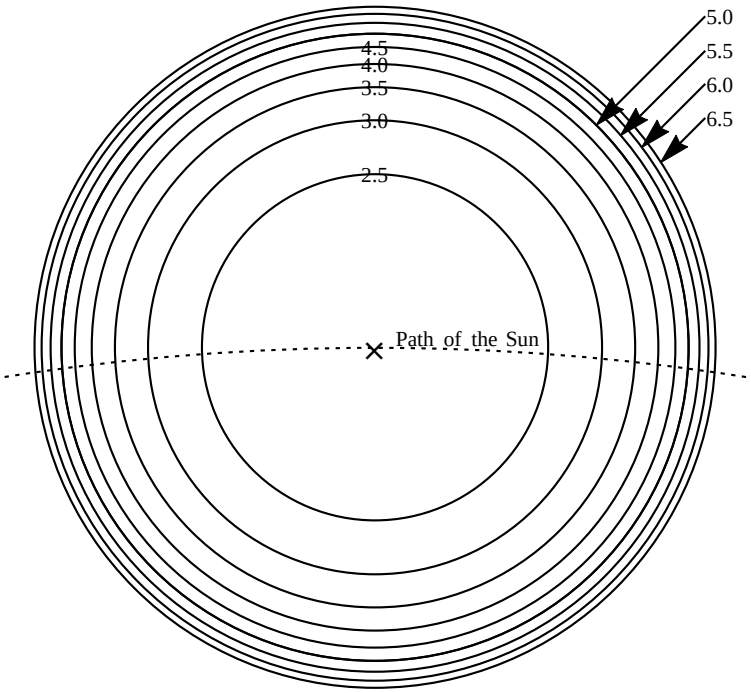

Figure 2.8: Isodetection contours projected on the celestial sphere for the $\boldsymbol{G} = 2\pi(\frac{1}{a}, \frac{1}{a}, \frac{1}{c})$ plane. The cross at the center is the projection of the normal to the (1,1,1) plane. The dotted trojectory represents the path of the Sun through that region [26].

from 2.5 keV to 6.5 keV for $\boldsymbol{G} = 2\pi(\frac{1}{a}, \frac{1}{a}, \frac{1}{c})$ in steps of 0.5 keV. The energy bin width is chosen to be slightly larger than the resolution of the detector. The cross at the center is the projection of $\boldsymbol{G}$ and the dotted trojectory represents a typical path of the Sun through that region. To give the reader some quantitative feeling for the angular size of the isodetection rings, the outermost ring at 6.5 keV has an angular radius of 72° and the ring for 6.0 keV has a radius of 70.5°, so the outermost annulus is 1.5° wide. The counting rate in the energy bin $6.0 - 6.5$ keV will rise when the Sun passes through this annulus, which takes about six minutes because the Sun angle moves 0.25°/min. As the Sun continues along its path, the counting rate in the next annulus, with energy $5.5 - 6.0$ keV, will increase, while the counting rate in the previous annulus will drop [26].

From figure 2.7 one can see that the complexity and sharpness of the counting rate

increases with energy. This is a geometric effect because, as is clear from figure 2.8, the Sun spends more time in the annuli corresponding to lower energies than those with corresponding to higher energy, and because there are many more reciprocal vectors available satisfying the Bragg condition. So the daily temporal pattern is dependent on how the Sun passes through those annuli. Figure 2.8 shows the Sun passing along a diameter and through all eight annuli, so one could expect the peaks to be seen in all energy bins in a symmetrical pattern. On the other hand the Sun might pass at a grazing trajectory that crosses the outer rings without going through the inner ones, so the patterns shown in one energy bin may not be seen in other energy bins [26].

2.4 Bound on Axion Mass

Axion mass dependent solar axion flux

Raffelt [60, 32] derived a formula to calculate the transition rate of a photon to an axion

$$\Gamma_{\gamma\to a} = \frac{T_\odot \kappa^2 g_{a\gamma\gamma}^2}{32\pi^2} \frac{|\boldsymbol{p}_\gamma|}{E_\gamma} \int \frac{|\boldsymbol{p}_\gamma \times \boldsymbol{p}_a|^2}{q^2\,(q^2+\kappa^2)} d\Omega \tag{2.51}$$

where $T_\odot$ is the temperature of solar core and $T_\odot = 15.6 \times 10^6\ K \Rightarrow 1.3$ keV, κ is the $Debye - H\ddot{u}ckel$ scale and is approximately 9 keV and $\boldsymbol{q}$ is the momentum transfer given by $\boldsymbol{q} = \boldsymbol{p}_\gamma - \boldsymbol{p}_a$. Vogel[76] has calculated the total rate with the result

$$\begin{aligned}\Gamma_{\gamma\to a} = &\frac{T_\odot \kappa^2 g_{a\gamma\gamma}^2}{32\pi^2} \times \frac{(m_a^2-\kappa^2)^2 + 4E_a^2\kappa^2}{4E_a p_a \kappa^2} \log\left[\frac{(E_a+p_a)^2+\kappa^2}{(E_a-p_a)^2+\kappa^2}\right] \\ &- \frac{T_\odot \kappa^2 g_{a\gamma\gamma}^2}{32\pi^2} \times \left(\frac{m_a^4}{4E_a p_a \kappa^2} \log\left[\frac{(E_a+p_a)^2}{(E_a-p_a)^2}\right] - 1\right)\end{aligned} \tag{2.52}$$

For axions with negligible mass, $p_a \approx E_a$, the next to the last term vanishes and Eq.(2.52) reduces to

$$\Gamma_{\gamma\to a} = \frac{T_\odot \kappa^2 g_{a\gamma}^2}{32\pi^2} \left[\left(1+\frac{\kappa^2}{4E^2}\right) \log\left(1+\frac{4E^2}{\kappa^2}\right) - 1\right] \tag{2.53}$$

The ratios of Eq.(2.53) over Eq.(2.52) as a function of the axion mass m_a, for different photon energies, are analyzed to determine the effect of the axion mass on the transition rate, as shown in Figure 2.9. The change of the transition rate due to axion mass is less than 3% for axion mass less than 1 keV.

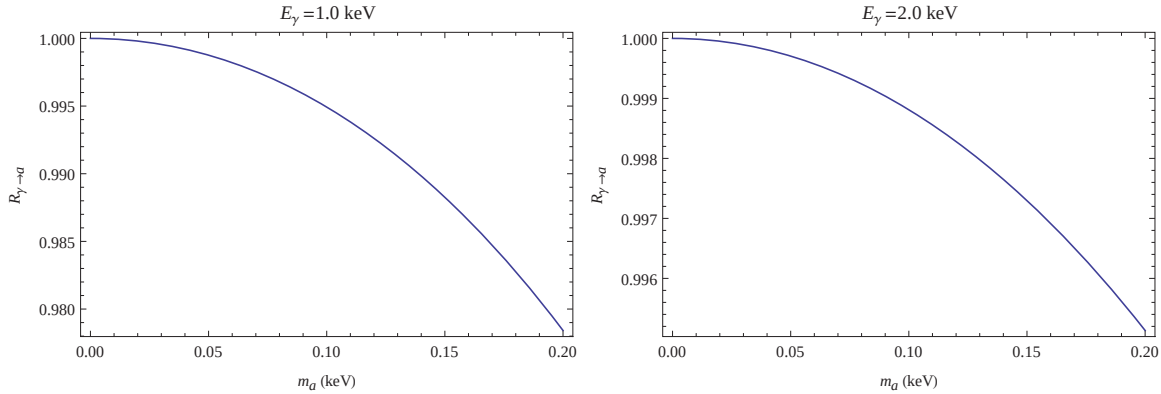

(a) $E_\gamma = 1$ keV (b) $E_\gamma = 2$ keV

Figure 2.9: Ratio of Eq.(2.53) over Eq.(2.52) for different photon energies. It can be used to determine the effect of the axion mass on the transition rate.

Decoherence length

The distance, over which the axion and photon remain coherent is given approximately by

$$(\boldsymbol{k}_\gamma - \boldsymbol{k}_a) \cdot \boldsymbol{d} \approx \pi \tag{2.54}$$

where $\boldsymbol{k}_\gamma - \boldsymbol{k}_a$ is the momentum transfer. For an axion with energy E, mass m and momentum $\hbar\boldsymbol{k}_a$, one has

$$E^2 = (m_a c^2)^2 + (\hbar c \boldsymbol{k}_a)^2 \tag{2.55}$$

which gives, for $E >> m_a c^2$,

$$\hbar c \boldsymbol{k}_a \approx E - \frac{(m_a c^2)^2}{2E}$$

Substituting this back to Eq.(2.54), and assuming that the energy of photon is equal to that of axion, gives

$$d = \frac{2\pi\hbar c E}{(m_a c^2)^2} \tag{2.56}$$

For an axion with energy 2 keV and mass 100 eV, the coherence length is ($\hbar c = 1.97\ keV \cdot$ Å)

$$\begin{aligned} d &= \frac{2\pi \times 1.97\ keV \cdot \text{Å} \times 2\ keV}{(0.1\ keV)^2} \\ &= 2475.58\ \text{Å} \end{aligned} \tag{2.57}$$

which is about 350 times bigger than the lattice constants ($a = b = 4.8088$ Å and $c = 7.6038$ Å [20]). So decoherence will not be an issue. We take 100 eV as an upper limit for the axion mass, which is somewhat arbitrary and conservative. The Bragg conversion probability is not very sensitive to axion masses less than 100 eV, and solar axion flux also varies very little. For axion masses of several hundred eV the solar axion spectrum is distorted and decoherence begins to affect the conversion probability.

2.5 14.4 keV solar axions emitted from the ground-state M1 transition of ^{57}Fe nuclei

Using Eq. (2.39) and Eq. (2.43), the cross section for a conversion of an axion to a photon by the inverse Primakoff effect is

$$\sigma_{a\gamma\gamma} = m\hbar^3 c^3 \frac{4\pi^2 \alpha N_a}{\mu_c v_c} g_{a\gamma\gamma}^2 \sum_{\boldsymbol{G}} |\tilde{\rho}_c(\boldsymbol{G})|^2 \frac{|\boldsymbol{p} \times \boldsymbol{G}|^2}{G^6} W_\Delta[E - E(\hat{\boldsymbol{p}}, \boldsymbol{G})] \tag{2.58}$$

For the solar axions emitted in the M1 transition of ^{57}Fe nuclei, the flux is approximated by[6]

$$\Phi_{Fe} = 4.56 \times 10^{27} (g_{an}^{eff})^2 / m^2 / s \tag{2.59}$$

where g_{an}^{eff} is the axion-nucleon coupling constant. So the total conversion rate of axions from M1 transition of ^{57}Fe nuclei to photons detected by the inverse Primakoff

conversion becomes

$$
\begin{aligned}
R_{Fe} &= \Phi_{Fe} \times \sigma_{a\gamma\gamma} \\
&= 4.56 \times 10^{27} (g_{an}^{eff})^2 \times m\hbar^3 c^3 \frac{4\pi^2 \alpha N_a}{\mu_c v_c} g_{a\gamma\gamma}^2 \sum_{\boldsymbol{G}} |\tilde{\rho}_c(\boldsymbol{G})|^2 \frac{|\boldsymbol{p} \times \boldsymbol{G}|^2}{G^6} W_\Delta[E - E(\hat{\boldsymbol{p}})] \\
&= 4.56 \times 10^{27} \times (g_{an}^{eff} g_{a\gamma\gamma})^2 m\hbar c \frac{4\pi^2 \alpha N_a}{\mu_c v_c} \sum_{\boldsymbol{G}} |\tilde{\rho}_c(\boldsymbol{G})|^2 E^2 \frac{|\hat{\boldsymbol{p}} \times \boldsymbol{G}|^2}{G^6} W_\Delta[E - E(\hat{\boldsymbol{p}})]
\end{aligned}
\tag{2.60}
$$

Figure 2.10 shows the expected counting rate of the 14.4 keV solar axions as a function of time over a single day.

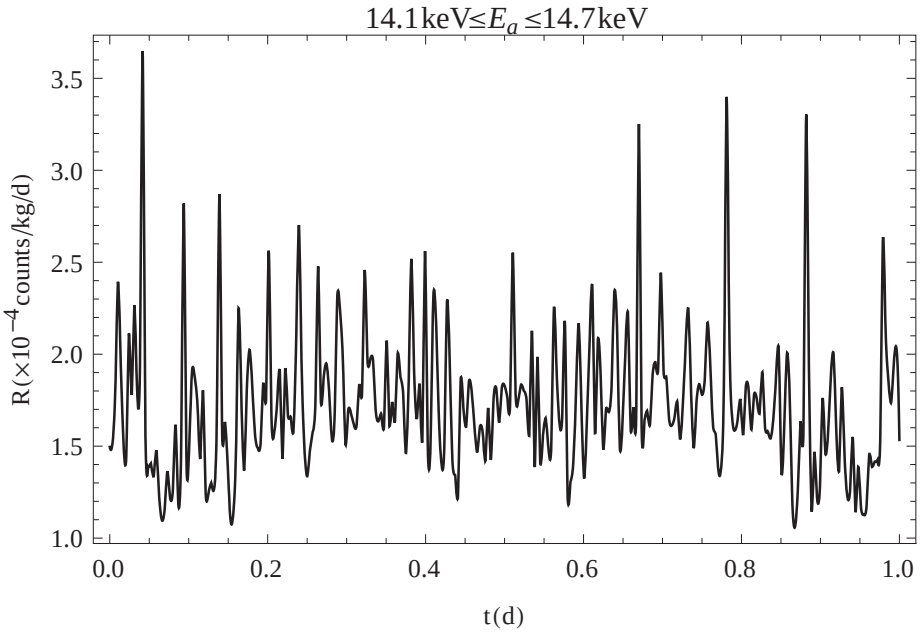

Figure 2.10: Expected counting rates $R(t)$ of photons produced by the inverse Primakoff conversion of 14.4 keV solar axions in the CUORE detector for $g_{a\gamma\gamma} g_{an}^{eff} = 1.105 \times 10^{-16}\ GeV^{-1}$.

Chapter 3

The CUORE Project

3.1 Introduction to CUORE

CUORE, which means "heart" in Italian, is an acronym for Cryogenic Underground Observatory for Rare Events, located in one of the the world's biggest underground laboratories focusing on subatomic particles. It is located at the Laboratori Nazionali del Gran Sasso(LNGS) in central Italy, between Rome and Adriatic Sea. The laboratory is built underneath the Gran Sasso mountain which provides a shield from cosmic radiation by 1400 meters of rock, or approximately 3650 meter water equivalent(3650 m.w.e). Consequently, the flux of cosmic rays, mainly muons and neutrons, can be greatly reduced to 2.85 ± 10^{-8} $\mu/cm^2/s$ and 4×10^{-6} $n/cm^2/s$[17], respectively. In addition, γ-rays with energies less than 3 MeV have a flux of 0.73 $\gamma/cm^2/s$. Although the primary goal of CUORE is to search for neutrinoless double beta decay($0\nu\beta\beta$), which could prove the Majorana nature of the neutrino, i.e., that the neutrino is its own antiparticle($\nu = \bar{\nu}$)[11][38], it may also give information about the neutrino mass hierarchy and absolute mass scale. CUORE also aims to be sensitive enough to search for dark matter and solar axions.

3.2 CUORE Detector and Cryostat

The CUORE detector is composed of 19 closely packed towers designed to operate at a very low temperature(10mK). Each tower has 13 floors, with four 5x5x5 cm^3 TeO_2 crystals (750 g each) on each floor, as seen in figure 3.1. There are 988 crystals

with a total mass of 741 kg of TeO_2 (204 kg of ^{130}Te). Tellurium was selected for two

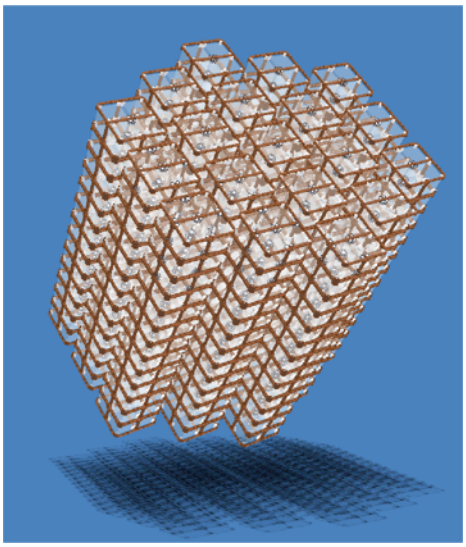

Figure 3.1: Drawing of the CUORE detector array: a cylindrical structure of 19 closely packed towers [22].

specific reasons: (1) it has a large natural abundance of the double beta decay isotope ^{130}Te at 34.2%[49];(2) it has a relatively high Q-value at 2528 keV[65][67][62]. The frame of the detector is made of an ultra-pure copper and the crystals are held by polytetrafluoroethylene (PTFE) brackets. In order to validate the feasibility of this ambitious project, two initial experiments, CUORICINO and CUORE-0 have been conducted in Hall A of LNGS to measure the background rate and energy resolution of the detector[34, 11].

Figure 3.2 shows a schematic of the CUORE cryostat. There are 6 thermal shields at 300 K, 40 K, 4 K, 800 mK, 50 mK and 10 mK. The 300 K and 4 K shields are vacuum chambers that allow the use of exchange gas in the inner vacuum chamber during the initial stage of cooling. Cryostat flanges that are made of Cu-OFE or Cu NOSV are fixed in place with a dedicated hoist system to lower and raise the shields. The entire cryostat with 1 ton of detector, 8 tons of thermal shields and flanges and 10 tons of the internal lead shielding, is suspended from a main support plate. Independent suspension systems for the vessels, dilution unit and detector are

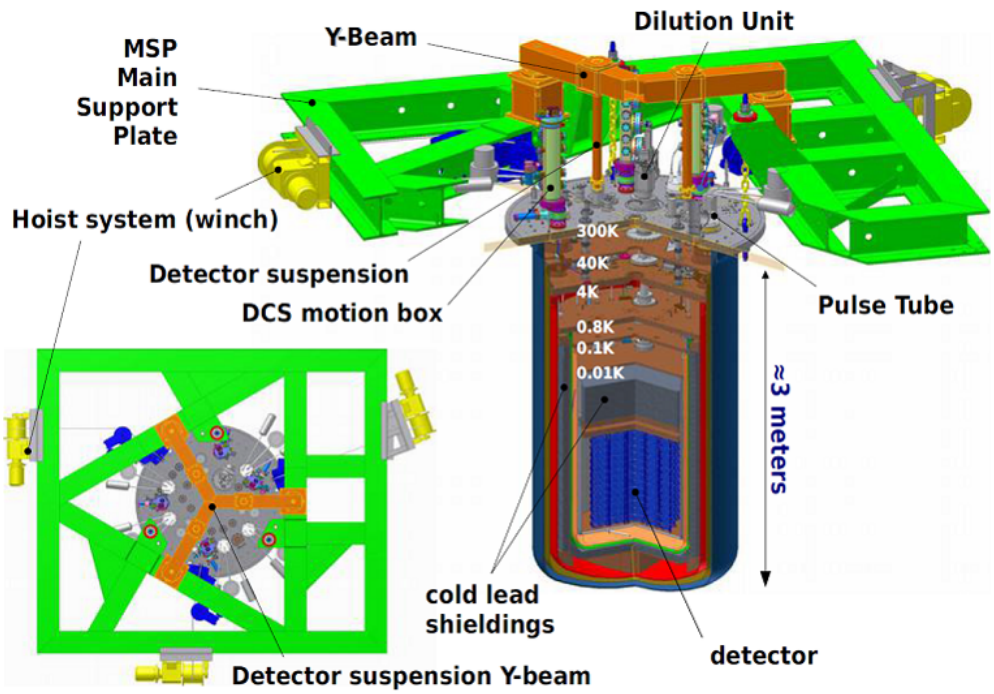

Figure 3.2: Schematic of the CUORE cryostat [22].

used to minimize vibrational noise of the detector.

Figure 3.3 shows the cold lead shieding with two parts: the top lead shield and the lateral lead shield. Together with the external lead shield, it is designed to surround the detector with 30 cm of lead in all directions. The top lead located below the mixing chamber plate is made of modern lead (2745 kg) with 30 cm in thickness and can shield the detector from the upper cryostat. In order to shield the detector from ^{210}Pb in the top lead, a 10 cm thick ultra-pure copper disc is mounted below the top shield. The lateral lead is composed of several 6 cm thick annular sections of ancient Roman lead [3], which is salvaged from shipwrecks off the Sardinian coast and is ideal for low background experiments because of the low activity of ^{210}Pb (< 4 mBq/kg). Figure 3.4 shows comparisons of spectra in the low energy region with shields made with different types of lead [3]. Three cooling methods are used to cool down such a large mass, pulse tube refrigerators, a dilution unit and a fast cooling system [22].

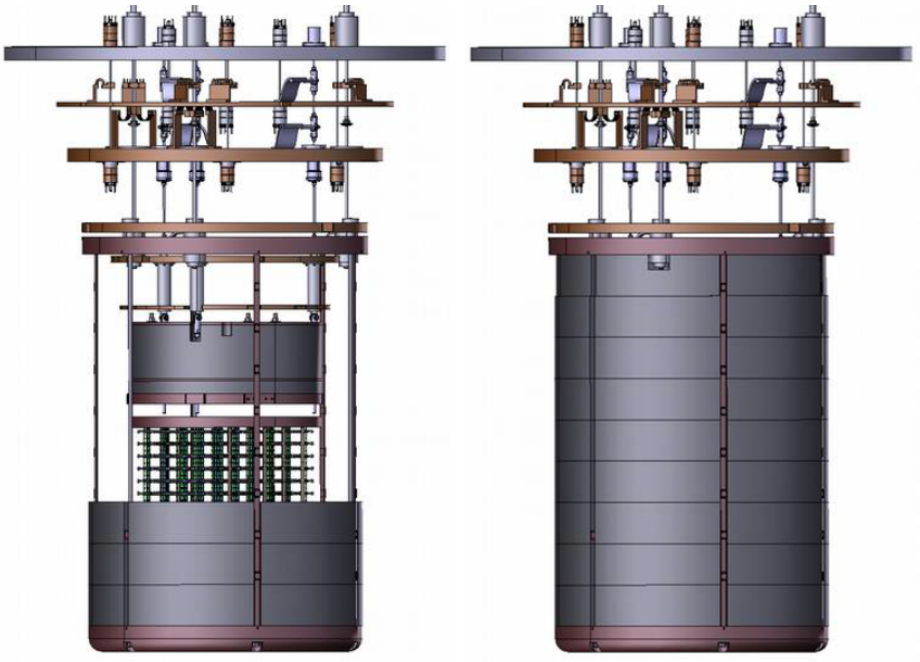

Figure 3.3: Schematic of the top and lateral cold lead shielding of the CUORE detector [22]

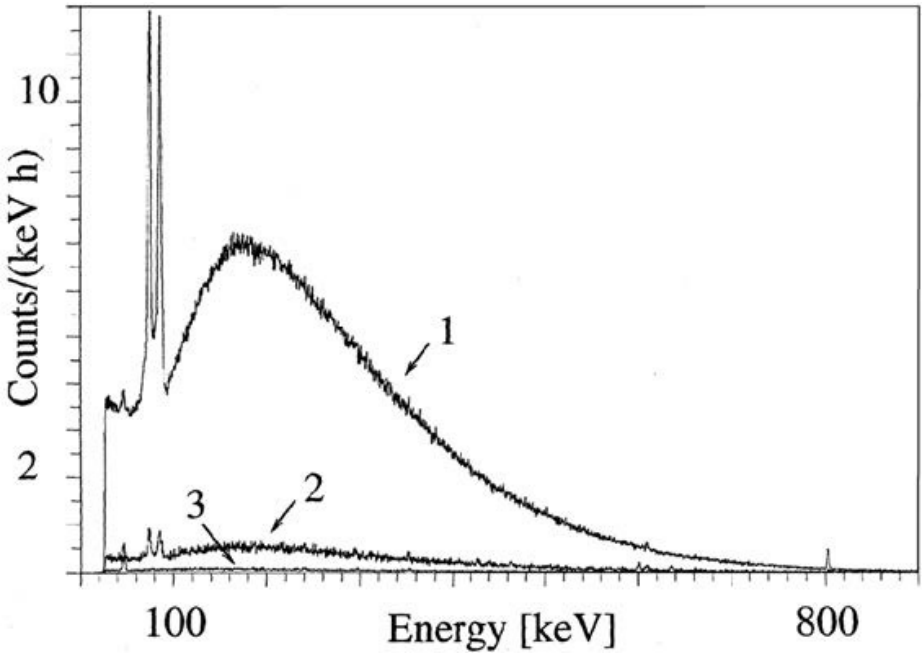

Figure 3.4: Spectra in the low energy region with shields made with different types of lead. 1. Comman modern lead; 2. Modern lead with a certified content of less than $20 Bq\ kg^{-1}\ ^{210}Pb$; 3. Roman lead from Oristano [3]

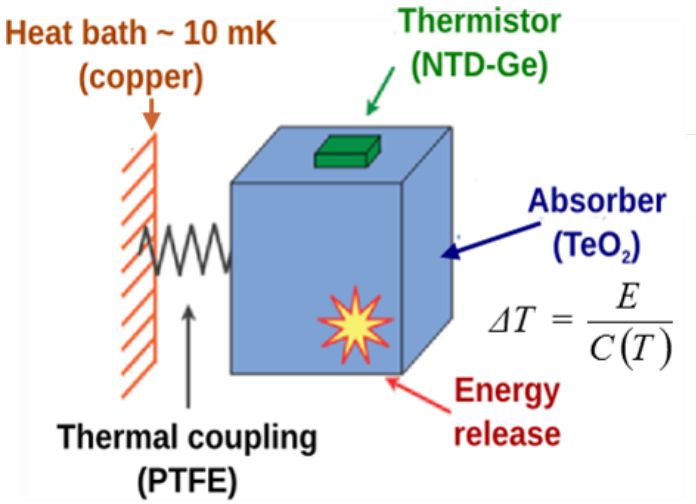

Figure 3.5: Schematic of a single CUORE bolometer [55]

3.3 Bolometric Technique

CUORE is a low temperature bolometric detector in which the source and the detector are the same. This "source = detector" technique ensures a high detector efficiency. A CUORE bolometer [74] is composed of two main parts, a TeO_2 crystal (absorber) and a neutron transmutation doped Germanium (NTD-Ge) thermistor. The TeO_2 crystal is held in place by PTFE supports in a copper frame, which is connected to the mixing chamber of a dilution refrigerator that keeps the bolometer at the operating temperature of $\sim$ 10 mK. The thermistor is glued to the crystal and works as a thermometer. Figure 3.5 and Figure 3.6 are two graphical representations of the bolometer. As shown in Figure 3.5, an incident particle deposits energy in the form of radiation in the crystal. The deposited energy is converted into phonons that cause an increase in temperature, which is measured by the decrease in the resistance of the thermistor. The thermistor is biased by a constant current and a change in the voltage across it gives the signal [4]. When operating properly, all energy is converted into heat and measured, giving a good energy resolution.

The bolometer technique is very sensitive to a tiny amount of energy deposited in the crystal. When an incident particle interacts with the crystal, phonons will be

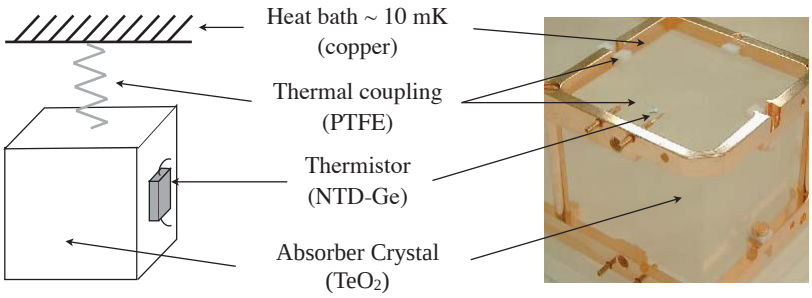

Figure 3.6: Bolometer sketch

produced out of equilibrium. Phonons then interact with other particles in the crystal and release their energy, resulting in a new distribution. The new distribution can be measured by a thermister as a temperature change based on the following expression:

$$\Delta T = \frac{\Delta E}{C} e^{-t/\tau} \tag{3.1}$$

where C is the heat capacity of the crystal and τ is the decay time constant for the pulse signal. The heat capacity of TeO_2 at low temperature T can be written as [31]

$$C(T) = \frac{12\pi^2}{5} k_B N_A \left(\frac{T}{T_D}\right)^3$$

where k_B is the Boltzmann constant and T_D is the Debye temperature and for TeO_2 $T_D \approx 232$ K. So C is very small because the operating temperature of the cryostat is at around 10 mK. Hence even a tiny change in energy can result in a measurable temperature change[55].

The bolometer technique can also give a fast signal response. Figure 3.7 shows a typical shape of a bolometer pulse with energy at around 2615 keV [4]. The rise time (from 10% to 90% of the maximum) is 0.04 s and the falling time (from 90% to 30% of maximum) is 0.26 s.

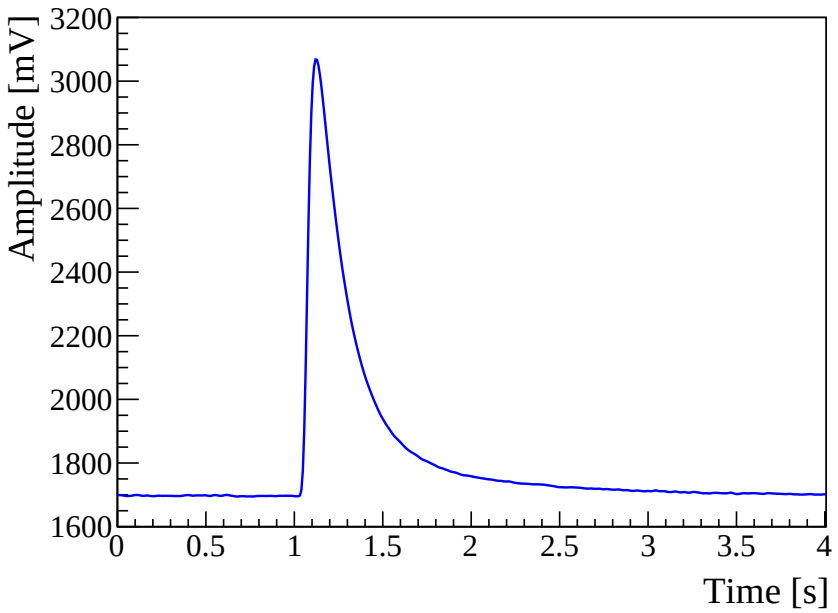

Figure 3.7: An example of a bolometer pulse with the energy of approximately 2615 keV [4]

In summary, the CUORE project and CUORE cryostat is specifically designed to overcome three main challenges: reduction of background rate through strict selection of location and cryostat materials, cooling down a large mass to the working temperature of 10 mK, while reducing the vibrational noise transmitted to the detector to ensure a better energy resolution, and bolometric technique to ensure a high detector efficiency and fast response.

Chapter 4

Data Analysis and Results

4.1 Pseudo Data Generation

Let R(t) be the instantaneous counting rate at time t. We assume that the detector runs from t_0 to $t + \Delta t$, where Δt is a small increment around t. The probability of no event during the time considered is

$$P_0(t + \Delta t, t_0) = P_0(t, t_0) \times (1 - R(t) \times \Delta t)$$

where $P_0(t, t_0)$ is the probability that no event occurs between the time interval t_0 and t. Rearranging the above equation gives the differential equation for $P_0(t, t_0)$

$$\frac{dP_0(t, t_0)}{dt} = -P_0(t, t_0)R(t)$$

So the probability of no event in the time interval (t_0, t) is

$$P_0(t, t_0) = e^{-\int_{t_0}^{t} R(t')dt'} \tag{4.1}$$

The probability of an event occurring at time t_1 is equal to the product of the probability of no event from t_0 to t_1 and one event in a small time interval Δt around t_1:

$$P_1(t_1) = P_0(t_1, t_0)R(t_1)\Delta t = e^{-\int_{t_0}^{t_1} R(t')dt'} R(t_1)\Delta t \tag{4.2}$$

The probability of the next event occurring at $t_2 > t_1$ is

$$P_2(t_2) = P_0(t_2, t_1)R(t_2)\Delta t = e^{-\int_{t_1}^{t_2} R(t')dt'} R(t_2)\Delta t \tag{4.3}$$

Figure 4.1 shows a characteristic counting rate of solar axions over a single day in the energy interval 2.5 keV $\leq E \leq$ 3.0 keV. One wants to generate a random sequence of

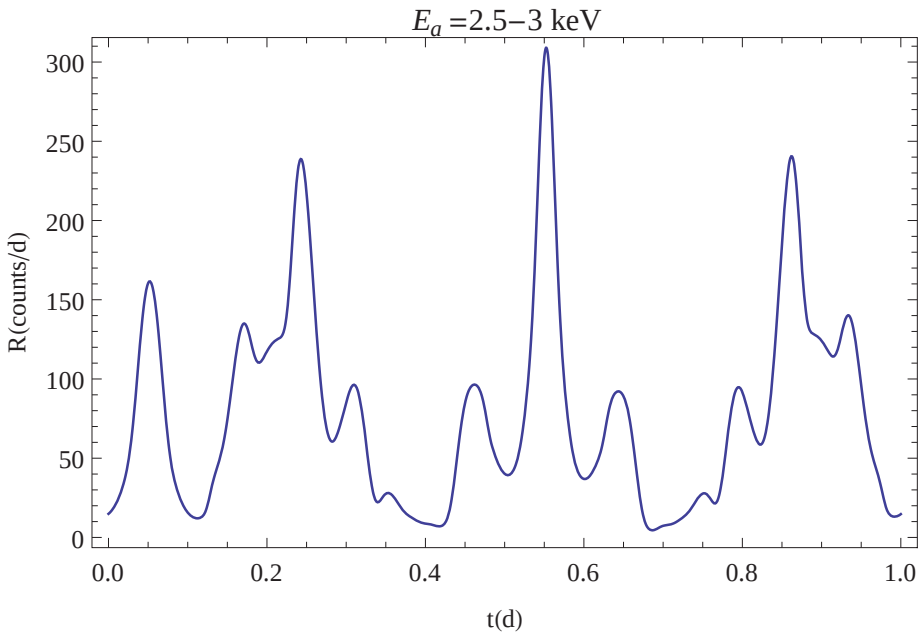

Figure 4.1: Characteristic counting rate of axion-photon conversion by the Primakoff coherent conversion in the crystal.

events that follows the counting rate R(t). Now consider the function

$$F(t) = 1 - e^{-\int_0^t R(t')dt'} \tag{4.4}$$

$F(t)$ will be in the interval $0 \leq F(t) \leq 1$. Suppose one can generate a pseudo-random number ρ of uniformly distributed on the interval $0 \leq \rho \leq 1$ and assign it to $F(t)$. The probability of choosing a random number ρ in a small interval $\Delta\rho$ is equal to the probability of finding an event at t_1 in a small time interval Δt

$$\Delta\rho = P_1(t_1)\Delta t$$

Differentiating $F(t)$ gives

$$\Delta F(t) = \Delta\rho = P_0(t, 0)R(t)\Delta t$$

Hence the time of the first event will be distributed correctly by solving $F(t_1) = \rho_1$, the the time of the second event will be distributed correctly by solving $F(t_2) = \rho_2$ and so on for a sequence of uniformly distributed random numbers $\{\rho_i, i = 1, 2, \cdots, N\}$.

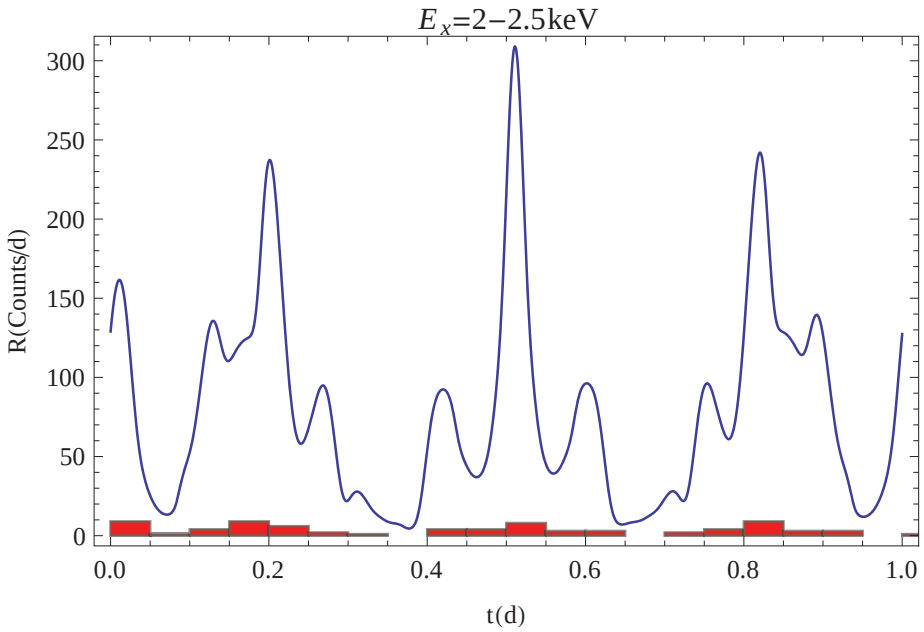

Figure 4.2: Histogram of random numbers generated by $F(t)$ with 20 bins overlaid by the corresponding R(t)

Note that the starting time used to solve $F(t) = \rho$ is t_0, which is time the first event occurs. In practice, ρ is generated by the software package used in our simulation, *Mathematica*. Each time a pseudo random number is generated, or an event occurs, the program calculates the time and sets it as the starting point for the next event until it reaches to the end of the time of simulation. Figure 4.2 shows the histogram event times generated by the above algorithm. Direct comparison of R(t) and the histogram plot shows that there is a direct correlation between the two figures: the number of events in an time interval Δt is proportional to $R(t)\Delta t$.

In order to generate a time sequence with enough length and simulate the real total counting rate, two modifications need to be performed. First, one needs to take into consideration the background counting rate in Gran Sasso. This can be done by adding in a constant number to the theoretical counting rate R(t). Second, one needs to keep track of the position of the Sun for the time length used in the simulation.The

total counting rate is:

$$R = R_{BG} + \lambda R_8(t) \tag{4.5}$$

where R_{BG} is the background counting rate which were taken to be 1 count/keV/kg/d[4], $\lambda R_8(t)$ is the theoretical counting rate of axions, and $\lambda = (g_{a\gamma\gamma} \times 10^{-8})^4$. For any fixed value of λ, we generate pseudo data accordingly and use to Time Correlation Method analyze the data set.

4.2 Time Correlation Method(TCM)

Assuming one has a set of data from the real experiment, which is composed of the background counting rate R_{BG} and the axion counting rate λR_8, one wants to extract useful information out of the entire data set and determine the real axion counting rate. Hence it would be best if one can cancel the influence from the background counting rate and make the instant that one gets a real event stand out at the same time. This motivation can be realized by employing the weighting function, which is subject to the following two constraints:

$$\sum_{i=1}^{N} W(t_i)\Delta t = 0, \sum_{i=1}^{N} W^2(t_i)\Delta t < \infty \tag{4.6}$$

or

$$\int_0^T W(t_i)dt = 0, \int_0^t W^2(t)dt < \infty \tag{4.7}$$

when Δt is sufficiently small.

Suppose we choose a time interval when the detector is on, $0 \leq t \leq T$ and divide it into tiny increments of time width Δt such that the expected number of events in any one increment is always much less than one, $R(t)\Delta t \ll 1$. Define a random variable $n(t_i)$ for the i-th time increment such that

$$\langle n(t_i) \rangle = R(t_i)\Delta t$$

The probability distribution for $n(t_i)$ is Poisson, but by making the time interval very small the number of events in each time interval is either 0 or 1. Let

$$\chi = \sum_{i=1}^{N} W(t_i) n(t_i) \tag{4.8}$$

where $W(t_i)$ is a weighting function. The expectation of χ will be

$$\begin{aligned} \langle \chi \rangle &= \sum_{i=1}^{N} W(t_i) R(t_i) \Delta t \\ &= \int_0^T W(t) R(t) dt \end{aligned} \tag{4.9}$$

The variance of χ becomes

$$\begin{aligned} \Delta\chi^2 &= \langle \chi^2 \rangle - \langle \chi \rangle^2 \\ &= \sum_{i,j} W(t_i) W(t_j) (\langle n(t_i) n(t_j) \rangle - \langle n(t_i) \rangle \langle n(t_j) \rangle) \\ &= \sum_i W^2(t_i) \left[\langle n^2(t_i) \rangle - \langle n(t_i) \rangle^2 \right] \\ &= \sum_i W^2(t_i) \langle n(t_i) \rangle \\ &= \sum_i W^2(t_i) R(t_i) \Delta t \\ &= \int_0^T W^2(t) R(t) dt \end{aligned} \tag{4.10}$$

The third line of Eq.(4.10) follows from the statistical independence of events at different times, $\langle n(t_i) n(t_j) \rangle = \langle n(t_i) \rangle \langle n(t_j) \rangle$ if $i \neq j$. The fourth line follows from the fact that the number of events in the time interval at $t = t_i$ is governed by a Poisson distribution, and for a Poisson distribution $\Delta n^2 = \langle n \rangle$. We also take the limit $\Delta t \to 0$ in the last line of Eq. (4.10).

We want to choose the weighting function that maximizes $\langle \chi \rangle$ subject to the constraints in Eq. (4.7). Therefore we use the method of Lagrange multipliers to find the unconstrained maximum of the functional

$$\mathscr{F} = \langle \chi \rangle - \mu_1 \int_0^T W^2(t) dt - \mu_2 \int_0^T W(t) dt \tag{4.11}$$

Maximizing $\mathscr{F}$ with respect to W(t) gives us

$$\int_0^T (R(t) - 2\mu_1 W(t) - \mu_2)\, dt = 0 \tag{4.12}$$

where μ_1 and μ_2 are multipliers. So

$$W(t) = \frac{1}{2\mu_1}(R(t) - \mu_2) \tag{4.13}$$

While μ_2 can be determined by using the constraint that $\int_0^T W(t)dt = 0$

$$\int_0^T (R(t) - \mu_2)dt = 0 \Rightarrow \mu_2 = \bar{R}$$

Since we can always adjust the value of μ_1, we normalize the weighting function so that

$$W(t) = R_8(t) - \bar{R}_8(t) \tag{4.14}$$

where $R_8(t)$ is the counting rate at $g_{a\gamma\gamma} = 10^{-8}$ and $\bar{R}_8(t)$ is the average counting rate over the time considered . It can also be shown that this is the best weighting function. Let us go back to our initial assumption, the total counting rate Eq. (4.5)

$$R(t) = R_{BG} + \lambda R_8(t)$$

Assume that we have generated a certain amount of pseudo data based on this total counting rate R(t). Using the weighting function Eq. (4.14) derived above we have

$$\chi = \sum_{i=1}^{N} [R_8(t_i) - \bar{R}_8(t_i)] \times n(t_i) \tag{4.15}$$

The expected average of $n(t_i)$ over a small time interval Δt_i can be written as:

$$\langle n(t_i) \rangle = (R_{BG} + \lambda R_8(t_i))\Delta t_i \tag{4.16}$$

Since we are doing the summations over the pseudo data and Δt_i is small, $n(t_i)$ is essentially equal to 1 or 0. So

$$\begin{aligned} \chi &\equiv \sum_{i=1}^{N} [R_8(t_i) - \bar{R}_8(t_i)] \times n(t_i) \\ &= \sum_{i=1}^{N} W(t_i) n(t_i) \\ &= \sum_{j} W(\tau_j) \end{aligned} \tag{4.17}$$

where τ_j are the times when we have an event. The statistical average of χ is:

$$\begin{aligned}
\langle\chi(\lambda)\rangle \equiv \langle\chi\rangle &= \sum_{i=1}^{N} W(t_i)\langle n(t_i)\rangle \\
&= \sum_{i=1}^{N} W(t_i)[R_{BG} + \lambda R_8(t_i)]\Delta t_i \\
&= \sum_{i=1}^{N} W(t_i)[R_{BG} + \lambda R_8(t_i) - \lambda\bar{R}_8(t_i) + \lambda\bar{R}_8(t_i)]\Delta t_i \\
&= \lambda\sum_{i=1}^{N} W^2(t_i)\Delta t_i \\
&= \lambda\int_0^T \left(R_8(t) - \bar{R}_8(t)\right)^2 dt
\end{aligned} \tag{4.18}$$

In the last step we used the property of the weighting function that it has a zero mean

$$\sum_{i=1}^{N} W(t_i)\Delta t_i = 0$$

We also take the limit $\Delta t_i \to 0$ so the summation can be changed to an integral. The variance of χ is

$$\begin{aligned}
(\Delta\chi(\lambda))^2 &= \langle\chi^2\rangle - \langle\chi\rangle^2 \\
&= \sum_{i=1}^{N}\sum_{j=1}^{N} W(t_i)W(t_j)(\langle n(t_i)n(t_j)\rangle - \langle n(t_i)\rangle\langle n(t_j)\rangle) \\
&= \sum_{i=1}^{N}\sum_{j=1}^{N} W^2(t_i)(\langle n^2(t_i)\rangle - \langle n(t_i)\rangle^2) \\
&= \sum_{i=1}^{N}\sum_{j=1}^{N} W^2(t_i)\langle n(t_i)\rangle \\
&= R_{BG}\int_0^T \left(R_8(t) - \bar{R}_8(t)\right)^2 dt + \lambda\int_0^T \left(R_8(t) - \bar{R}_8(t)\right)^2 R_8(t)dt
\end{aligned} \tag{4.19}$$

Note that the uncorrelated events are canceled out in the second step. We also used the fact that those events satisfy Poisson statistics, so in the third step we have

$$\langle n^2(t_i)\rangle - \langle n(t_i)\rangle^2 = \langle n(t_i)\rangle \tag{4.20}$$

The second term in $\Delta\chi^2$ is negligible compared with the first term when λ is small, so

$$\Delta\chi^2 = R_{BG}\int_0^T \left(R_8(t) - \bar{R}_8(t)\right)^2 dt \tag{4.21}$$

Distribution Function for χ

The number of events in each time interval is statistically independent, so the probability distribution of χ for a given weighting function $W(t)$ is

$$P(\chi|W) = \left\langle \delta\left(\chi - \sum_{i=1}^{N} W(t_i)n(t_i)\right)\right\rangle \tag{4.22}$$

The delta function can be represented by its Fourier transform,

$$P(\chi|W) = \frac{1}{2\pi}\int_{-\infty}^{\infty} e^{-i\omega\chi}\prod_{i=1}^{N}\left\langle e^{i\omega W(t_i)n(t_i)}\right\rangle d\omega \tag{4.23}$$

Let us define:

$$g_i(\omega) = \left\langle e^{i\omega W(t_i)n(t_i)}\right\rangle$$

then

$$P(\chi|W) = \frac{1}{2\pi}\int_{-\infty}^{\infty} e^{-i\omega\chi}\prod_{i=1}^{N} g_i(\omega)d\omega \tag{4.24}$$

If we expand $g_i(\omega)$ in a Taylor series about $\omega = 0$, we have

$$\begin{aligned} g_i(\omega) &= 1 + i\omega W(t_i)\langle n_i\rangle - \frac{1}{2}\omega^2 W^2(t_i)\langle n_i^2\rangle + \cdots \\ &= \exp\left[i\omega W(t_i)R(t_i)\Delta t - \frac{1}{2}\omega^2 W^2(t_i)R(t_i)\Delta t\right] \end{aligned}$$

This then gives

$$\begin{aligned} P(\chi|W) &= \frac{1}{2\pi}\int_{-\infty}^{\infty}\exp\left[-i\omega(\chi - \langle\chi\rangle) - \frac{1}{2}\omega^2\Delta\chi^2\right]d\omega \\ &= \frac{1}{\sqrt{2\pi\Delta\chi^2}}\exp\left[-\frac{(\chi - \langle\chi\rangle)^2}{2\Delta\chi^2}\right] \end{aligned} \tag{4.25}$$

where in the last step we completed the square. This shows that the probability distribution for χ for a given weighting function $W(t)$ is a Gaussian. And we just proved the Central Limit Theorem(CLT), which states that quantities which are functions of many small and uncorrelated random variables are approximately normally distributed. In an experiment, each event is an independent random variable and uncorrelated with other events, so the distribution of χ should have the same expression as Gaussian distribution. The log likelihood function for λ is

$$L(\lambda) \propto -\frac{\left(\chi - \lambda\int W(t)(R_8 - \bar{R}_8)dt\right)^2}{2R_{BG}\int W^2(t)dt} \tag{4.26}$$

The most probable value for λ is

$$\bar{\lambda} = \frac{\langle \chi \rangle}{\int W^2(t)dt} \tag{4.27}$$

The width of the likelihood function is

$$\Delta\lambda^2 = \frac{R_{BG} \int W^2(t)dt}{\left(\int W(t)\left(R_8(t) - \bar{R}_8\right)dt\right)^2} \tag{4.28}$$

Taking the variational derivative with respect to W then gives

$$\frac{\delta\Delta\lambda^2}{\delta W(t)} \propto \frac{W(t)\int W(t')(R_8(t') - \bar{R}_8)dt' - (R_8(t) - \bar{R}_8)\int W^2(t')dt'}{\left(\int W(t)(R_8(t) - \bar{R}_8)dt\right)^3} \tag{4.29}$$

which vanishes if $W = R_8 - \bar{R}_8$. With this choice of weighting function

$$\Delta\lambda = \sqrt{\frac{R_{BG}}{\int W^2(t)dt}} \tag{4.30}$$

If we choose the weighting function to be eq. (4.14), not only is $\langle \chi \rangle$ maximized but also $\Delta\lambda$ is minimized. The generalization to the case with several independent energy bins is straightforward; eq. (4.27) becomes

$$\bar{\lambda} = \frac{\sum_k \langle \chi_k \rangle}{\sum_k \int W_k^2(t)dt} \tag{4.31}$$

and eq. (4.30) becomes

$$\Delta\lambda = \sqrt{\frac{R_{BG}}{\sum_k \int W_k^2(t)dt}} \tag{4.32}$$

where k is the index for the energy bins. The relationship between $\Delta\lambda$ and time length T can be calculated as following. From the previous weighting function calculation, we have

$$\Delta\lambda = \frac{1}{\sqrt{T}}\sqrt{\frac{R_{BG}}{\int_0^1 W^2(t)dt}} \tag{4.33}$$

which is what we expected: the longer time the detector is on, the more real events we have, hence we can get a more accurate result.

Simulation Results

From last section we have:

$$P(\chi|W) = \frac{1}{\sqrt{2\pi\Delta\chi^2}} \exp\left[-\frac{(\chi - \langle\chi\rangle)^2}{2\Delta\chi^2}\right]$$

Maximizing $P(\chi)$ with respect to λ we can get the calculated λ. Table 4.1 is the simulation result for $\lambda = 1$ with time length 10 days, 30 days and 90 days, respectively.

Table 4.1: $4.5 - 5keV$, $\lambda = 1$, TCM, 741 kg

T(d)	Number of Events	Calculated λ	FWHM	M
10	6682	0.9493	0.05874	1.0228×10^8
30	20305	1.0047	0.04410	0.9913×10^8
90	60592	1.0012	0.01947	0.9988×10^8

In order to verify that the $P(\lambda)$ at the calculated λ is maximized, we plot a normalized graph of $P(\lambda)$ VS λ. Figure 4.3 is the comparison plots with 10 days counts, 30 days and 90 days, respectively. The error bar, $\Delta\lambda$ Eq. (4.33) can be

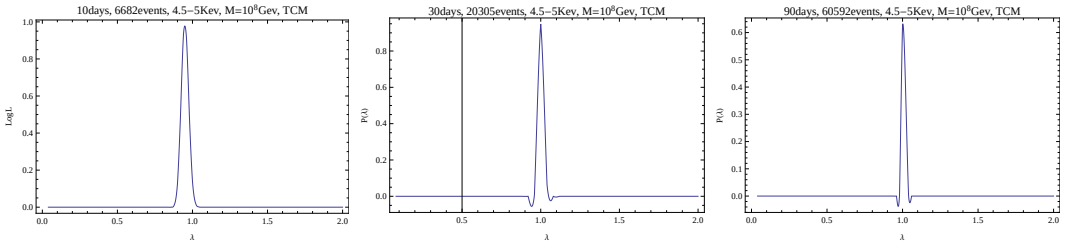

(a) 10 days (b) 30 days (c) 90days

Figure 4.3: Comparison between plots

written as:

$$\Delta\lambda = \frac{1}{\sqrt{T}} \sqrt{\frac{R_{BG}}{\int_0^1 W^2(t)dt}} \tag{4.34}$$

For a given time length, this value is fixed. Table 4.2 shows the calculation results for CUORE while keeping it runing for a whole year.

Figure 4.4 is a plot of simulated results of λ_s VS λ, where λ_s is the simulated result of a given λ. The straight line besecting the first and third quadrants is the

Table 4.2: Simulation results for 741 kg·year of exposure of the CUORE detector.

λ	Numerical Value	λ_s	$\Delta\lambda$
$\frac{1}{8^4}$	2.441×10^{-4}	5.56×10^{-4}	2.269×10^{-3}
$\frac{1}{9^4}$	1.524×10^{-4}	2.031×10^{-4}	2.269×10^{-3}
$\frac{1}{10^4}$	1.0×10^{-4}	1.752×10^{-4}	2.269×10^{-3}
$\frac{1}{11^4}$	6.83×10^{-5}	-8.72×10^{-4}	2.269×10^{-3}
$\frac{1}{12^4}$	4.82×10^{-5}	2.05×10^{-4}	2.269×10^{-3}
$\frac{1}{13^4}$	3.5×10^{-5}	1.2×10^{-4}	2.269×10^{-3}

ideal result with $\lambda_s = \lambda$, where λ_s is the simulated result. The error bar is calculated based on Eq. (4.33) with $T = 1$ year. Figure 4.5 is a band plot of this simulation result, which is more clear and readable compared with the error bar plot. The top and bottom dashed lines represent plus or minus one sigma, $\Delta\lambda$. The one nearest to the origin is out of the band because of the length of time. Taking into account of the statistical uncertainty, we can see that all simulations are in the range of the error bar and our calculation is statistically reliable.

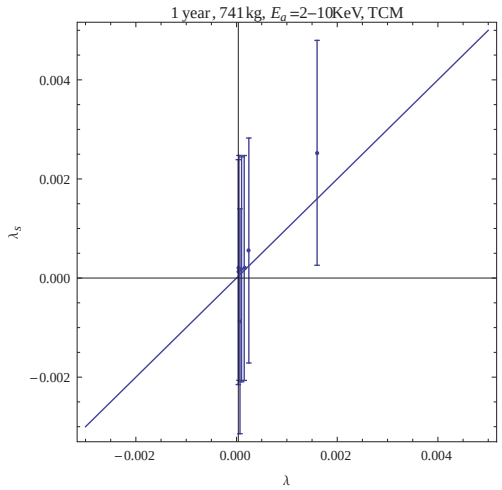

Figure 4.4: Plot of λ_s VS λ.

Figure 4.6 and Figure 4.7 show us the simulation results as a function of a given set of λ with increment of time length. The error bar shrinks and the error band gets narrowers as we increase the time length, which is what we expected based

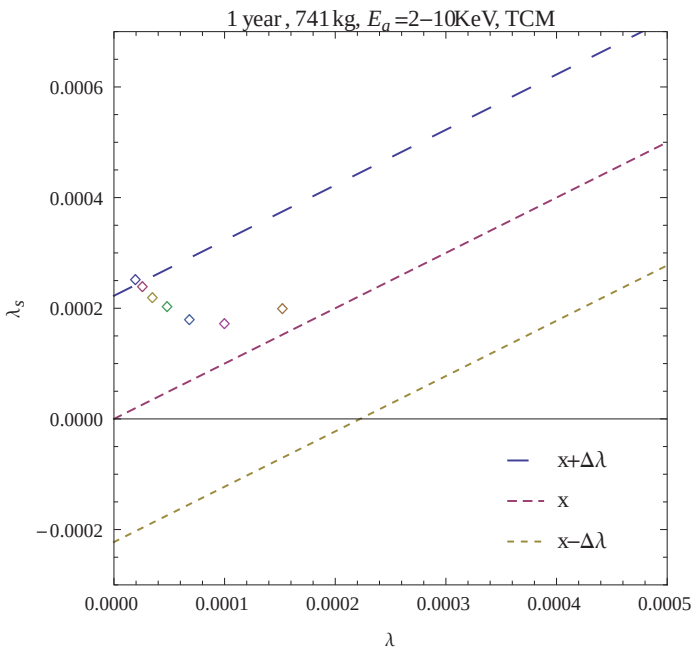

Figure 4.5: Band plot of 741 kg·year of exposure for the CUORE detector.

on our calculation. But for a fixed length of time, there is a lower bound on λ from simulations. This can be explained by the fact that the background radiation dominates the total event rate and the ratio of real events to background radiation will become smaller as we decrease the value of λ. So we need to operate the detector on for a longer time if we want to be sensitive to a smaller value of λ, or we can increase the mass of the detector, both of which will give us a sensitivity to smaller λ, thus pushing down the limit on the coupling constant $g_{a\gamma\gamma}$.

4.3 Effect of Detector Rotations with Respect to Z-axis

When the crystals used by CUORE are grown and cut finally, we know crystal axes. And crystals will be aligned properly when CUORE is constructed. When the Y-axis is pointing east and Z-axis upward. So there is no need to place a constraint on the conversion rate. But when the detector is rotated by a certain angle, will this rotation cause any effect in our calculation? And how large is this effect? This is a good question to ask.

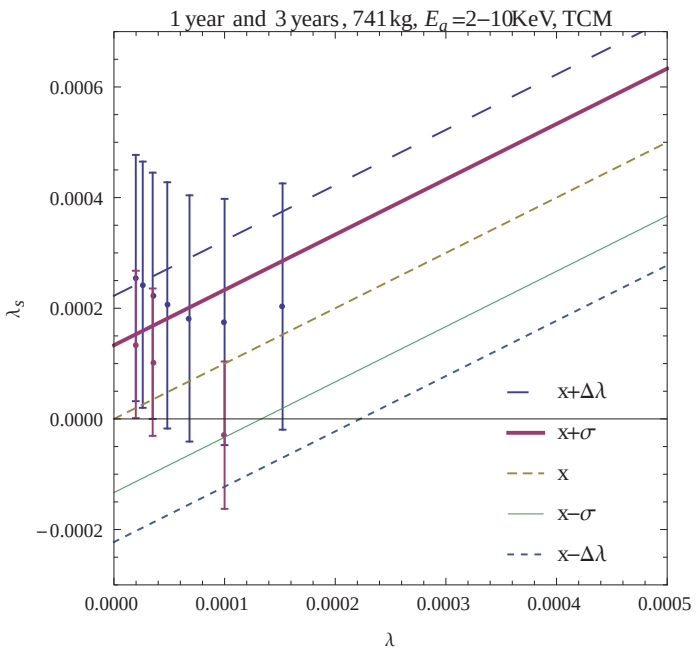

Figure 4.6: Simulation results for the CUORE detector with different exposure time for a given set of λ.

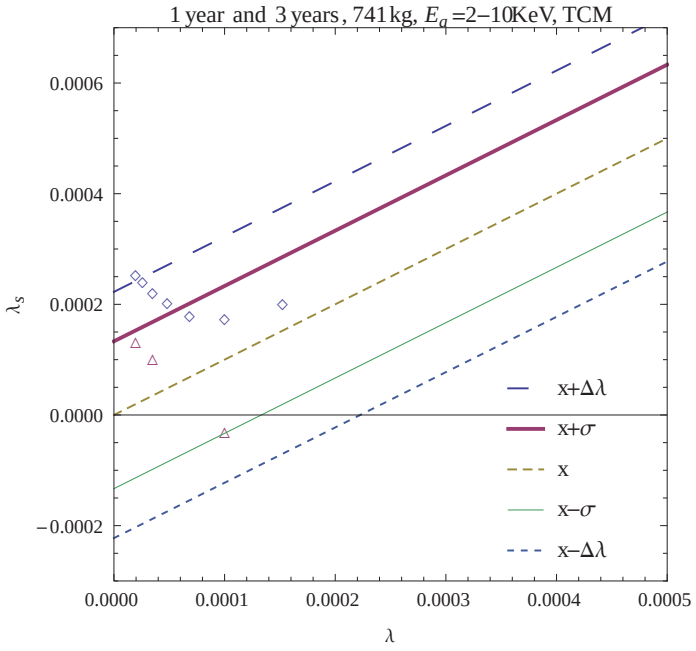

Figure 4.7: Band plot of the simulation results with respect to exposure time 1 year and 3 year, respectively.

To determine the effect brought about by rotating the detector by mistake, we calculated the counting rates with different degrees of rotations with respect to Z-

axis. Note that rotating the detector is equivalent to shifting the Sun's azimuthal angle by the same amount, clockwise or counterclockwise, depending on the direction of rotation. Then we calculated λ by using Time Correlation Method. It should be pointed out that the weighting function used here is still the same weighting function used before, which is different from these shifted counting rates. Below is the detailed changes in the calculation:

$$W(t) = R(t) - \bar{R}(t) \rightarrow W(t) = R(t) - \bar{R}(t) \tag{4.35}$$

$$\chi = \sum_{t_i}(R(t_i) - \bar{R}(t_i)) \times n(t_i) \rightarrow \chi_{rt} = \sum_{t_i}(R(t_i) - \bar{R}(t_i)) \times n_{rt}(t_i) \tag{4.36}$$

$$\langle\chi(\lambda)\rangle = \sum_{t_i} W(t_i)[R_{BG} + \lambda R(t_i)]\Delta t_i \rightarrow \langle\chi_{rt}(\lambda)\rangle = \sum_{t_i} W(t_i)[R_{BG} + \lambda R_{rt}(t_i)]\Delta t_i \tag{4.37}$$

$$\Delta\chi^2(\lambda) = \sum_{t_i} W^2(t_i)[R_{BG} + \lambda R(t_i)]\Delta t_i \rightarrow \Delta\chi^2_{rt}(\lambda) = \sum_{t_i} W^2(t_i)[R_{BG} + \lambda R_{rt}(t_i)]\Delta t_i \tag{4.38}$$

where the subscript "rt" designates the counting rates with rotated detector. The detector is rotated intentionally by 0°, 1°, 3°, 5°, 10°respectively. Then counting rates are generated accordingly. The calculated λ and FWHM are shown in Table 4.3: where ϕ is the azimuthal angle of the Sun and FWHM is the full width at half

Table 4.3: Rotated detector results.

ϕ	λ	FWHM
0°	1.00322	0.1606
1°	0.94815	0.1606
3°	0.66895	0.1606
5°	0.38572	0.1606
10°	−1.88424	N/A

maximum. From these results it is easy to arrive at two conclusions. First, when the detector is rotated by 10°, we have a negative λ, which means that the counting rate at 10°rotation of detector is anti-correlated with our initial counting rate. Since the

two rates are anti-correlated, this can explain why we couldn't get a corresponding FWHM. Second, the FWHMs are the same for the rest of rotated angles. This seems bizarre at the first look, but if we go back to our $\Delta\chi^2$ calculation:

$$\Delta\chi^2(\lambda) = \sum_{t_i} W^2(t_i)[R_{BG} + \lambda R(t_i)]\Delta t_i \tag{4.39}$$

when λ is small, the background counting rate dominates the result of $\Delta\chi^2(\lambda)$, so the contribution from the second term is negligible. That's why we could have the same FWHM. Figure 4.8 shows the comparisons among different angles. Because $\Delta\lambda^2$ is

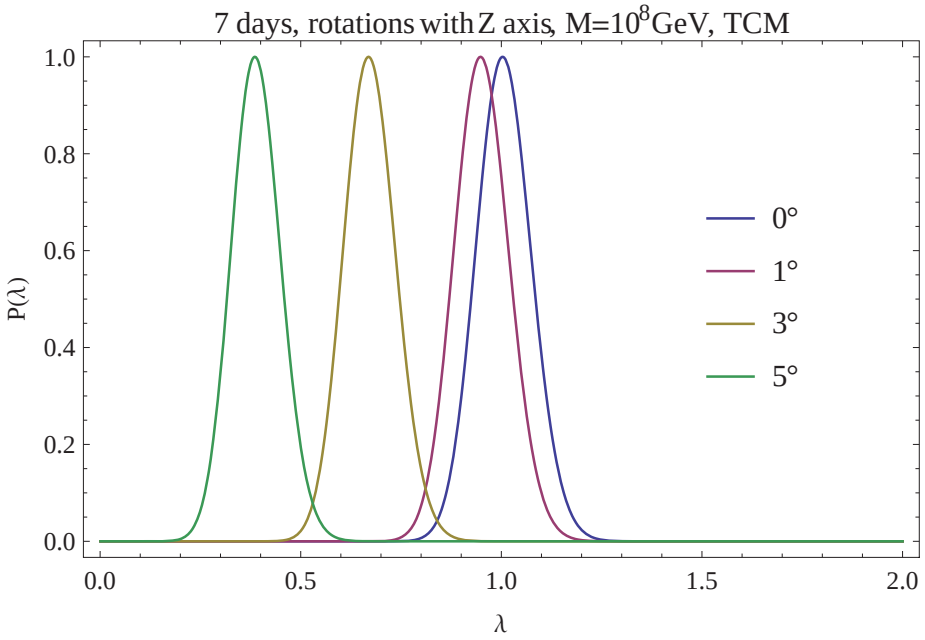

Figure 4.8: Comparison of values of P(λ) for various angles of rotation of the detector.

inversely proportional to the integral of the weighting functions squared

$$\Delta\lambda^2 = \frac{R_{BG}}{\int_0^T W^2(t)dt} \tag{4.40}$$

Another way to understand the correlation between the counting rate with unrotated detector and the one with rotated detector is to compare the weighting functions of the two rates at different angles. We define

$$Ratio = \frac{\int_0^1 W_o W_\varphi dt}{\int_0^1 W_0^2 dt} \tag{4.41}$$

where W_0 is the weighting function for the unrotated detector and W_φ the weighting function for the rotated detector with rotation angle φ. Figure 4.9 shows a plot of the "Ratio" as a function of detector angle rotation. The correlation between the two drops down fast and reaches to a minimum at around 10°, which in turn will give us a significant change in the results calculated by the time correlation method and hence make it impossible to use. However, detector rotated by 10° is very large and the detector position in φ must be controlled to within 1°.

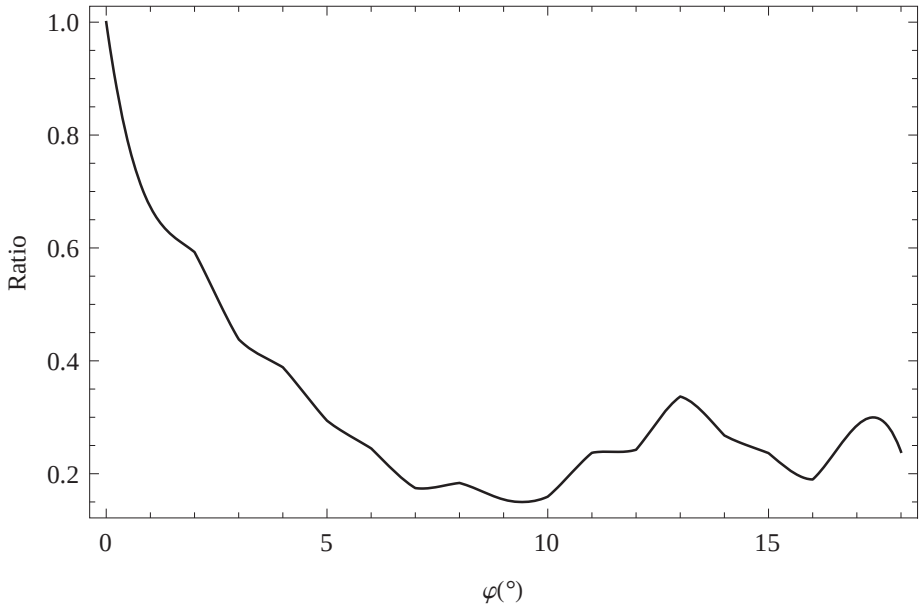

Figure 4.9: Comparison of Ratios given by Eq. (4.41) with different rotation angles φ

Chapter 5

Conclusion

The times produced by the pseudo-data generation process $\{t_i, i = 1, \cdots, N\}$ are used to calculate $\chi = \sum_{i=1}^{N} W(t_i)$, and from this we extract $\bar{\lambda}$ and $\Delta\lambda$ as described in previous chapters.

5.1 Coupling Constant $g_{a\gamma\gamma}$

Extensive Monte Carlo calculation have been carried out using the mass, energy resolution and realistic background for the CUORE detector operating for 5 years. The results show that the CUORE detector with 741 kg TeO_2 in operation for 5 years can set an upper bound on λ of

$$\lambda < 2.15 \times 10^{-6} \tag{5.1}$$

which is equivalent to an upper limit on the axion-photon coupling constant $g_{a\gamma\gamma} < 3.83 \times 10^{-10}$ at 95% confidence level. To illustrate the resolving power of the time correlation method, in five years with $g_{a\gamma\gamma} = 3.83 \times 10^{-10}$ there are approximately 600 events due to axion conversion and 5.5×10^5 background events [26].

Figure 5.1 is an exclusion plot comparing this calculation with the best limits set by CAST [81, 5, 8] on the $g_{a\gamma\gamma}$-m_a plane. The lightly shaded area and dotdashed line correspond to various theoretical axion models [40, 68, 80, 28]. Our predicted bound is comparable to the newest CAST results for axions with mass less than 1.2 eV [8] and will improve the bound for axion masses in the range 1 $eV \leq m_a \leq$ 100 eV [1],

[1]The upper limit of 100 eV is somewhat arbitrary and conservative. The Bragg conversion

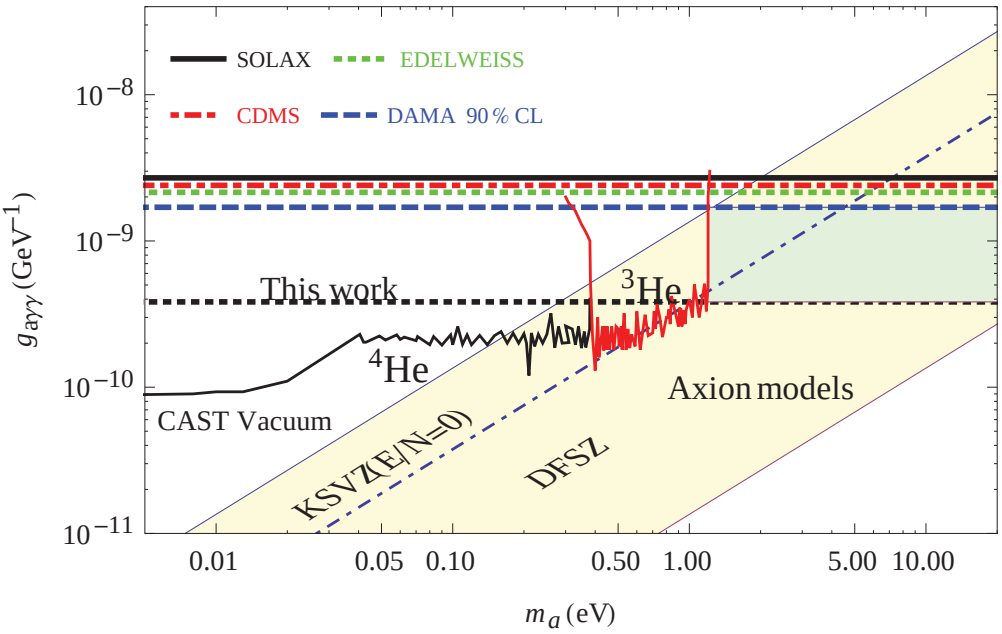

Figure 5.1: Exclusion limits on the $g_{a\gamma\gamma}$-m_a plane. The shaded area is favored by the KSVZ [40, 68] and the DFSZ [80, 28] axion models. The dotted line shows that with 3705 kg y of data, CUORE could exclude axions with $g_{a\gamma\gamma} > 3.83 \times 10^{-10}\ GeV^{-1}$ and masses less than 100 eV [26].

indicated by the darker shaded region(green in color) [26].

Recently, the International Axion Observatory (IAXO), a new generation axion helioscope searching for solar axions by Primakoff conversion in a strong magnetic field, has been proposed (see recent work by J. K. Vogel et al. [75]). The predicted sensitivity of IAXO to the coupling constant $g_{a\gamma\gamma}$ is predicted to be on the order of $4 \times 10^{-12}\ GeV^{-1}$ for axion masses less than 0.1 eV. This is a great improvement over all current experiments, narrowing down the search region for axions and dark matter significantly. However, this excluded region of parameter space will not reach beyond 0.2 eV [26].

probability is not very sensitive to axion masses less than 100 eV, and solar axion flux also varies very little. For axion masses of several hundred eV the solar axion spectrum is distorted and decoherence begins to affect the conversion probability.

5.2 Product of the axion-photon coupling and the axion-nucleon coupling $g_{a\gamma\gamma}g_{aN}^{eff}$

The time correlation of individual events with the theoretical time-dependent counting rate is also used to calculate the sensitivity of the CUORE detector to $g_{a\gamma\gamma}g_{aN}^{\rm eff}$[26]. The limit on the axion mass m_a is calculated by reevaluating $\delta(E_a - E_\gamma)$ in Eq. (2.19), in which we assumed that the mass of the axion is negligible compared with its energy. And the momentum transfer $\boldsymbol{p} - \boldsymbol{k}$ needs to satisfy $\boldsymbol{p} - \boldsymbol{k} = \boldsymbol{G}$. The Bragg condition

$$E(\hat{\boldsymbol{p}}, \boldsymbol{G}) = \hbar c \frac{G^2}{2\hat{\boldsymbol{p}} \cdot \boldsymbol{G}} \tag{5.2}$$

must be satisfied by the energy of the axion and direction to the Sun $\hat{\boldsymbol{p}}$ in order to have coherent conversion of axions to photons. If the axion has a mass m_a the Bragg condition in Eq. (5.2) is modified to

$$E(\hat{\boldsymbol{p}}, \boldsymbol{G}) = \sqrt{\hbar^2 c^2 \left(\frac{G^2 - m^2}{2\hat{\boldsymbol{p}} \cdot \boldsymbol{G}} \right)^2 + m_a^2 c^4} \tag{5.3}$$

For axion masses less than 500 eV the shift in the Bragg peaks and the flux from the Sun are changed by only 1.56 %. For axion masses approaching 1 keV these effects become more pronounced, so we place an arbitrary and conservative limit on the axion mass of 500 eV.

The Monte Carlo simulation for 741 kg y can set a model-independent upper bound for the product of the axion-photon and the axion-nucleon coupling constants $g_{a\gamma\gamma}g_{aN}^{\rm eff} < 2.47 \times 10^{-16}$ GeV^{-1}. To illustrate the resolving power of the time correlation method for the 14.4 keV solar axions, there are approximately 300 events due to axion conversion and 1.05×10^5 background events in one year with $g_{a\gamma\gamma}g_{aN}^{\rm eff} = 2.47 \times 10^{-16}$ GeV^{-1}. With five years of data, CUORE can set an upper bound of $g_{a\gamma\gamma}g_{aN}^{\rm eff} < 1.105 \times 10^{-16}$ GeV^{-1}, which is slightly better than the current bound set by CAST for $m_a < 0.03$ eV, as shown in Figure 5.2. For ten years simulation, the upper bound can be reached to $g_{a\gamma\gamma}g_{aN}^{\rm eff} < 0.781 \times 10^{-16}$ GeV^{-1} [47]. Figure 5.3 shows the excluded

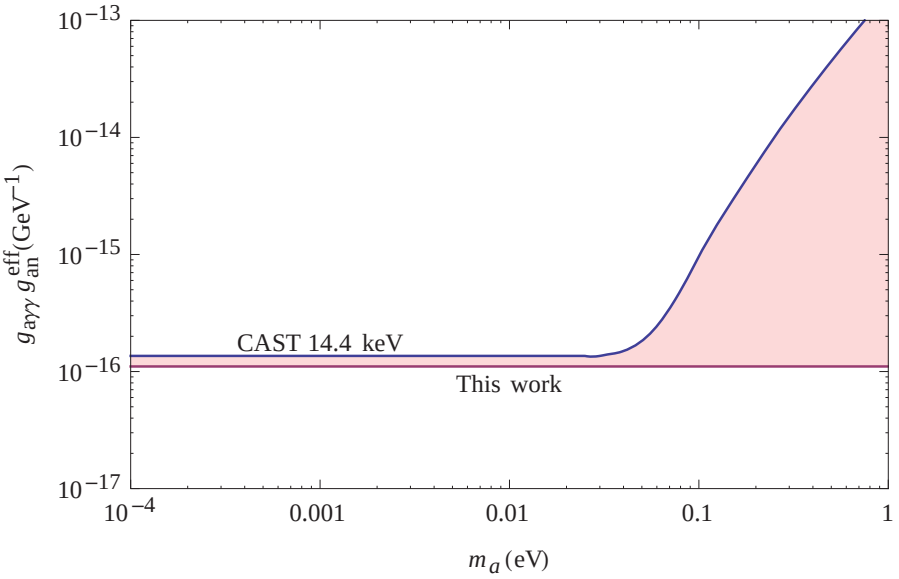

Figure 5.2: Exclusion limits one the $g_{a\gamma\gamma}g_{an} - m_a$ plane. The shaded region is that which CUORE could exclude for axion masses less than 500 eV, that were not excluded by CAST [47].

region of the $g_{a\gamma\gamma} - m_a$ plane achieved by CAST assuming $g_{an} = 3.6 \times 10^{-6}$, which is set by the requirement that the ^{57}Fe solar axion luminosity should be less than 10% of the solar photon luminosity($L_a < 0.1 L_\odot$)[56]. The dotted line is a bound for $g_{a\gamma\gamma}$ that could be set by CUORE under the same assumption. Our simulation shows that CUORE could eliminate a substantial part of the model space not yet touched by other experiments.

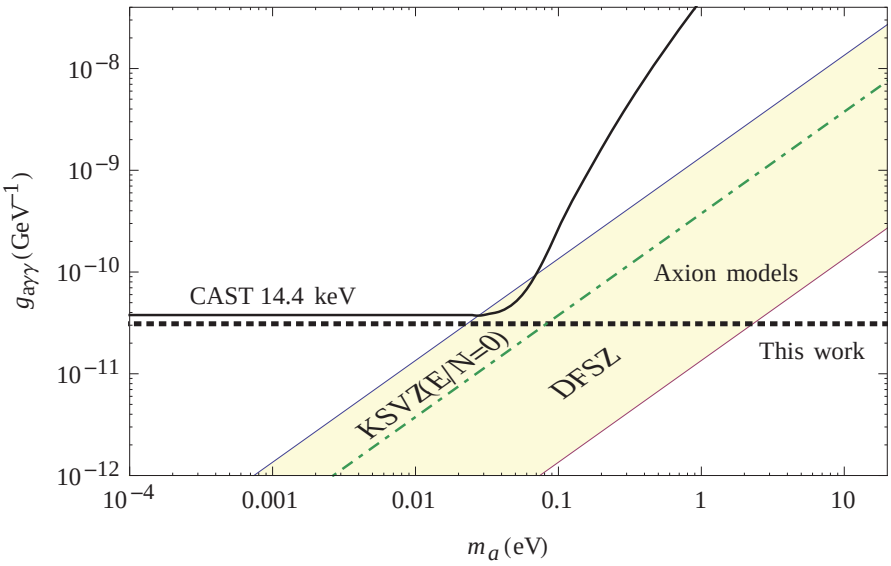

Figure 5.3: Predicted exclusion limits on the $g_{a\gamma\gamma} - m_a$ plane that could be placed by CUORE. The dotted line is a relative limit on the $g_{a\gamma\gamma}$ coupling constant with $g_{an} = 3.6 \times 10^{-6}$ [6].

Bibliography

[1] L. F. Abbott and P. Sikivie, *A cosmological bound on the invisible axion*, Phys. Lett. B **120** (1983), 133.

[2] Z. Ahmed et al., *Search for Axions with the CDMS Experiment*, Phys. Rev. Lett **103** (2009), 141802.

[3] A. Alessandrello, C. Arpesella, C. Brofferio, C. Bucci, et al., *Measurements of internal radioactive contamination in samples of roman lead to be used in experiments on rare events*, Nuclear Instruments and Methods in Physics Research B **142** (1998), 163–172.

[4] F. Alessandria et al., *The low energy spectrum of Teo_2 bolometers: results and dark matter perspectives for the CUORE–0 and CUORE experiments*, J. Cosmol. Astropart. Phys **038** (2013), 1475.

[5] S. Andriamonje, S. Aune, et al., *An improved limit on the axion–photon coupling from the CAST experiment*, J. Cosmol. Astropart. Phys **04** (2007), 010.

[6] S. Andriamonje et al., *Search for* 14.4 *keV solar axions emitted in the M1-transition of ^{57}Fe nuclei with CAST*, J. Cosmol. Astropart. Phys **002** (2009).

[7] R. Ardito et al., *CUORE: A Cryogenic Underground Observatory for Rare Events*, hep-ex/0501010 (2005).

[8] M. Arik et al., *Search for Solar Axions by the CERN Axion Solar Telescope with ^3He Buffer Gas: Closing the Hot Dark Matter Gap*, Phys. Rev. Lett **112** (2014), 091302.

[9] E. Armengaud et al., *Axion searches with the EDELWEISS-II experiment*, J. Cosmol. Astropart. Phys **11** (2013), 067.

[10] C. Arnaboldi et al., *CUORE: a cryogenic underground observatory for rare events*, Nucl. Instrum. Meth. A **518** (2004), 775.

[11] D. R. Artusa, F. T. Avignone III, O. Azzolini, M. Balata, T. I. Banks, G. Bari, J. Beeman, F. Bellini, et al., *Initial performance of the CUORE-0 experiment*, The European Physical Journal C **74** (2014), 2956.

[12] S. J. Asztalos et al., *An improved RF cavity search for halo axions*, Phys. Rev. D **69** (2004), 011101.

[13] F. T. Avignone, *Potential for large germanium detector arrays for solar-axion searches utilizing the axio-electric effect for detection*, Phys. Rev. D **79** (2009), 035015.

[14] F. T. Avignone, D. Abriola, R. L. Brodzinski, J. I. Collar, R. J. Creswick, et al., *Solar Axion Experiments Using Coherent Primakoff Conversion in Single Crystals*, Nuclear Physics B **72** (1999), 176–182.

[15] C. A. Baker, D. D. Doyle, et al., *An Improved experimental limit on the electric dipole moment of the neutron*, Phys. Rev. Lett **97** (2006), 131801.

[16] Augusto Barroso and Nimai C. Mukhopadhyay, *Axions: To Be Or Not To Be?*, Phys. Lett. B **106** (1981), 91–94.

[17] F. Bellini, Bucci, S. Capelli, O. Cremonesi, L. Gironi, M. Martinez, M. Pavan, C. Tomei, and M. Vignati, *Monte Carlo evaluation of the external gamma, neutron and muon induced background sources in the CUORE experiment*, Astroparticle Physics **33** (2010), 169–174.

[18] R. Bernabei, P. Belli, R. Cerulli, et al., *Search for solar axions by Primakoff effect in NaI crystals*, Phys. Lett. B **515** (2001), 6–12.

[19] R. Bradley et al., *Microwave cavity searches for dark-matter axions*, Rev. Mod. Phys **75** (2003), 777.

[20] C. Arnaboldi and others, *Measurement of Low Temperature Specific Heat of Crystalline Teo_2 for the Optimization of Bolometric Detectors*, Journal of Low Temperature Physics **123** (2001), 303.

[21] S. L. Cheng, C. Q. Geng, and W. T. Ni, *Axion-photon couplings in invisible axion models*, Phys. Rev. D **52** (1995), 3132.

[22] Nicholas I Chott, Franco Alessandria, Carlo Bucci, Paolo Gorla, Luigi Cappelli, Carmine Pagliarone, Carlo Ligi, Angelo Nucciotti, Francesco Terranova, and

Luca Taffarello, *Commissioning of the cuore cryostat: The first experimental setup for bolometric detectors at the 1 ton scale*, Proceedings of Technology and Instrumentation in Particle Physics 2014 (TIPP2014). 2-6 June 2014. Amsterdam, the Netherlands. Online at http://pos. sissa. it/cgi-bin/reader/conf. cgi? confid= 213, id. 217, vol. 1, 2014, p. 217.

[23] Richard Creswick, *Quantum Theory*, unpublished, 2011.

[24] R.J. Creswick, F.T. Avignone III, H.A. Farach, J.I. Collar, A.O. Gattone, S. Nussinov, and K. Zioutas, *Theory for the direct detection of solar axions by coherent primakoff conversion in germanium detectors*, Physics Letters B **427** (1998), 235.

[25] R. L. Davis, *Cosmic axions from cosmic strings*, Phys. Lett. B **180** (1986), 225.

[26] Dawei Li and Richard J. Creswick and Frank T. Avignone III and Yuanxu Wang, *Theoretical estimate of the sensitivity of the cuore detector to solar axions*, J. Cosmol. Astropart. Phys **10** (2015), 065.

[27] M. Dine and W. Fischler, *The not–so–harmless axion*, Phys. Lett. B **120** (1983), 137.

[28] M. Dine, W. Fischler, and M. Srednick, *A simple solution to the strong CP problem with a harmless axion*, Phys. Rev. Lett **104** (1981), 199.

[29] L. Duffy et al., *A high resolution search for dark-matter axions*, Phys. Rev. D **74** (2006), 012006.

[30] F. Alessandria and others, *Search for* 14.4 *keV solar axions from M1 transition of* ^{57}*Fe with CUORE crystals*, J. Cosmol. Astropart. Phys **05** (2013).

[31] E. Fiorini and T. Niinikoski, *Low-temperature calorimetry for rare decays*, Nuclear Instruments and Methods in Physics Research **224** (1984), 83.

[32] G. G. Raffelt, *Plasmon decay into low-mass bosons in stars*, Phys. Rev. D **37** (1988), 1356.

[33] J. Gasser and H. Leutwyler, *Quark masses*, Phys. Rept **87** (1982), 77.

[34] G. Gervasio et al., *Large Cryogenic Detector for Double Beta Decay, WIMPS and Solar Axions*, Nuclear Physics A **663&664** (2000), 873.

[35] G.K. White and S.J. Collocott and J.G. Collins, *Thermal properties of paratellurite (TeO_2) at low temperatures*, Journal of Physics: Condensed Matter **2** (1990), 7715.

[36] W. C. Haxton and K. Y. Lee, *Red-Giant Evolution, Metallicity, and New Bounds on Hadronic Axions*, Phys. Rev. Lett. **66** (1991), 2557.

[37] F. T. Avignone III et al., *Search for axions from the* 1115*-kev transition of* ^{65}Cu, Phys. Rev. D **37** (1988), 618.

[38] Frank T. Avignone III, Steven R. Elliott, and Jonathan Engel, *Double Beta Decay, Majorana Neutrinos, and Neutrino Mass*, Rev. Mod. Phys **80** (2008), 481–516.

[39] Y. Inoue et al., *Search for sub–electronvolt solar axions using coherent conversion of axions into photons in magnetic field and gas helium*, Phys. Lett. B **536** (2002), 18.

[40] J. E. Kim, *Weak interaction singlet and strong CP invariance*, Phys. Rev. Lett **43** (1979), 103.

[41] Jihn E. Kim, *Constraints on very light axions from cavity experiments*, Phys. Lett. D **28** (1998), 055006.

[42] L. M. Krauss and F. Wilczek, *A short-lived axion variant*, Phys. Lett. B **173** (1986), 189–192.

[43] M. Krcmar, Z. Krecak, A. Ljubicic, M. Stipcevic, and D. A. Bradley, *Search for solar axions using* ^7Li, Phys. Rev. D **64** (2001), 115016.

[44] M. Krcmar, Z. Krecak, M. Stipcevic, A. Ljubicic, and D. A. Bradley, *Search for solar axions using* ^{57} *Fe*, Phys. Lett. B **442** (1998), 38–42.

[45] D. M. Lazarus et al., *Search for solar axions*, Phys. Rev. Lett **69** (1992), 2333.

[46] H. Leutwyler, *The ratio of light quark masses*, Phys. Lett. B **378** (1996), 313.

[47] Dawei Li, Richard J. Creswick, Frank T. Avignone III, and Yuanxu Wang, *Sensitivity of the CUORE detector to* 14.4 *keV solar axions emitted by the M1 nuclear transition of* ^{57}Fe, J. Cosmol. Astropart. Phys **002** (2016), 031.

[48] A. Ljubicic, D. Kekez, Z. Krecak, and T. Ljubicic, *Search for hadronic axions using axioelectric effect*, Phys. Lett. B **B599** (2004), 143–147.

[49] A.N. Halliday M. A. Fehr, M. Rehkamper, *Application of MC-ICPMS to the precise determination of tellurium isotope compositions in chondrites, iron meteorites and sulfides*, Int. J. Mass spectrom **232** (2004), 83–94.

[50] M. Barucci and C. Brofferio and A. Giuliani and E. Gottardi and I. Peroni and G. Ventura, *Production of high purity TeO_2 single crystals for the study of neutrinoless double beta decay*, Journal of Crystal Growth **312** (2010), 2999.

[51] A. Morales, F. T. Avignone, et al., *Particle Dark Matter and Solar Axion Searches with a small germanium detector at the Canfranc Underground Laboratory*, Astropart. Phys **16** (2002), 325.

[52] S. Moriyama, *Proposal to Search for a Monochromatic Component of Solar Axions Using ^{57}Fe*, Phys. Rev. Lett. **75** (1995), 3222.

[53] Shigetaka Moriyama et al., *Direct search for solar axions by using strong magnetic field and X–ray detectors*, Phys. Lett. B **434** (1998), 147.

[54] T. Namba, *Results of a search for monochromatic solar axions using ^{57} Fe*, Phys. Lett. B **645** (2007), 398–401.

[55] Seth Newman, *Search for solar axions*, Ph.D. thesis, Podunk IN, 2011.

[56] P. Gondolo and G. G. Raffelt, *Solar neutrino limit on axions and keV-mass bosons*, Phys. Rev. D **79** (2009), 107301.

[57] R. D. Peccei, *The Strong CP problem and axions*, Axions: Theory, cosmology, and experimental searches. Proceedings, 1st Joint ILIAS-CERN-CAST axion training, Geneva, Switzerland, November 30-December 2, 2005, vol. 741, 2008, pp. 3–17.

[58] R.D. Peccei and H.Quinn, *Constraints imposed by CP conservation in the presence of pseudoparticles*, Phys. Rev. D **16** (1977), 1791–1797.

[59] J. Preskill, M. B. Wise, and F. Wilczek, *Cosmology of the invisible axion*, Phys. Lett. B **120** (1983), 127.

[60] G. G. Raffelt, *Astrophysical axion bounds diminished by screening effects*, Phys. Rev. D **33** (1986), 897.

[61] Georg G. Raffelt, *Axions: Motivation, limits and searches*, J. Phys. **A40** (2007), 6607–6620.

[62] S. Rahaman, V.V. Elomaa, T. Eronen, J. Hakala, A. Jokinen, A. Kankainen, J. Rissanen, J. Suhonen, C. Weber, and J. Aysto, *Double-beta decay Q values of Cd-116 and Te-130*, Phys. Lett. B **703** (2011), 412–416.

[63] R.D. Peccei and H.Quinn, *CP Conservation in the Presence of Pseudoparticles*, Phys. Rev. Lett **38** (1977), 1440–1443.

[64] Javier Redondo, *Solar axion flux from the axion-electron coupling*, J. Cosmol. Astropart. Phys **008** (2013), 1312.

[65] Matthew Redshaw, Brianna J. Mount, Edmund G. Myers, and Frank T. Avignone III, *Masses of 130Te, 130Xe and double-beta-decay Q-value of 130Te*, Phys. Rev. Lett **102** (2009), 212502.

[66] R. Rodenberg S. Barshay, H. Faissner and H. de Witt, *Coherent Conversion of Very Light Pseudoscalar Bosons*, Phys. Rev. Lett **46** (1981), 1361.

[67] N. D. Scielzo, S. Caldwell, G. Savard, J. A. Clark, C. M. Deibel, J. Fallis, S. Gulick, D. Lascar, A. F. Levand, G. Li, J. Mintz, E. B. Norman, K. S. Sharma, M. Sternberg, T. Sun, and J. Van Schelt, *Double-beta decay Q values of 130Te, 128Te, and 120Te*, Phys. Rev. C **80** (2009), 025501.

[68] M. A. Shifman, A. I. Vainshtein, and V. I. Zakharov, *Can confinement ensure natural CP invariance of strong interactions?*, Nucl. Phys. B **166** (1980), 493.

[69] P. Sikivie, *Experimental Tests of the "Invisible" Axion*, Phys. Rev. Lett **51** (1983), 1415–1417.

[70] Steven Weinberg, *A New Light Boson?*, Phys. Rev. Lett **40** (1978), 223.

[71] G. 't Hooft, *Symmetry Breaking through Bell-Jackiw Anomalies*, Phys. Rev. Lett **37** (1976), 8.

[72] R. S. Lytel R. D. Peccei T. W. Donnelly, S. J. Freedman and M. Schwartz, *Do axions exist?*, Phys. Rev. D **18** (1978), 1607.

[73] K. van Bibber, P. M. McIntyre, D. E. Morris, and G. G. Raffelt, *Design for a practical laboratory detector for solar axions*, Phys. Rev. D **39** (1989), 2089.

[74] Marco Vignati, *Model of the Response Function of Large Mass Bolometric Detectors*, Journal of Applied Physics **108** (2010), 084903.

[75] J. K. Vogel et al., *The next generation of axion helioscopes: The International Axion Observatory (IXAO)*, Physics Procedia **61** (2015), 193.

[76] Julia Katharina Vogel, *Searching for Solar Axions in the eV-Mass Region with the CCD Detector at CAST*, Ph.D. thesis, Freiburg, Germany, 2009.

[77] Steven Weinberg, *The U(1) problem*, Phys. Rev. D **11** (1975), 3583.

[78] F. Wilczek, *Problem of Strong P and T Invariance in the Presence of instantons*, Phys. Rev. Lett **40** (1978), 279–282.

[79] W. M. Yao et al., *Review of Particle Physics*, Journal of Physics G: Nuclear and Particle Physics **33** (2006), 1.

[80] A. R. Zhitnitsky, *On possible suppression of the axion–hadron interactions*, Sov. J. Nucl. Phys **31** (1980), 260.

[81] K. Zioutas et al., *First results from the CERN axion solar telescope (CAST)*, Phys. Rev. Lett **94** (2005), 121301.